Bioinorganic Chemistry

International Edition: DOI: 10.1002/anie.201907502
German Edition: DOI: 10.1002/ange.201907502

Catalysis and Electron Transfer in De Novo Designed Helical Scaffolds

*Tyler B. J. Pinter, Karl J. Koebke, and Vincent L. Pecoraro**

Keywords:
enzymes · helical structures · metalloproteins · protein design · transition metals

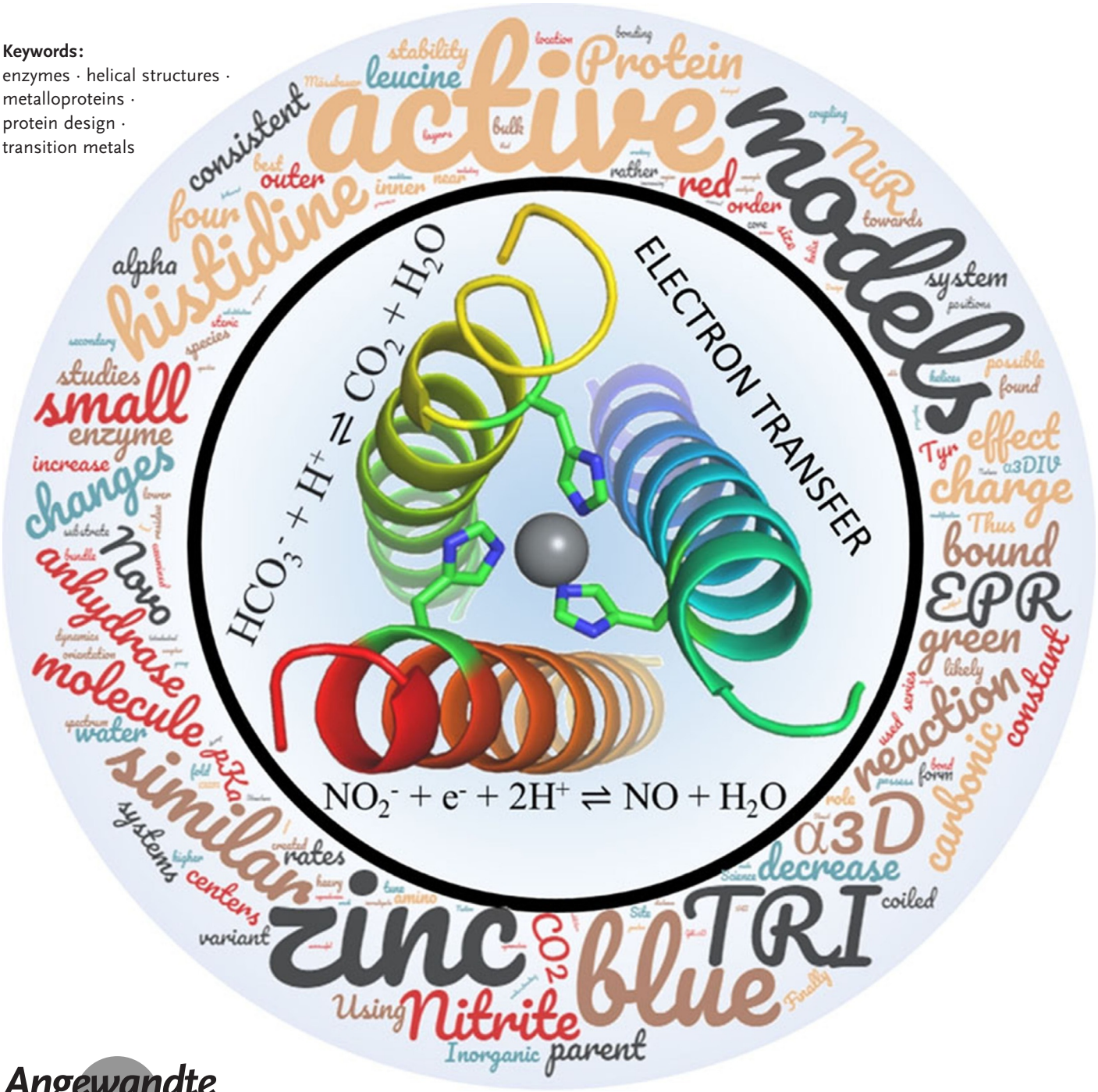

The relationship between protein structure and function is one of the greatest puzzles within biochemistry. De novo metalloprotein design is a way to wipe the board clean and determine what is required to build in function from the ground up in an unrelated structure. This Review focuses on protein design efforts to create de novo metalloproteins within alpha-helical scaffolds. Examples of successful designs include those with carbonic anhydrase or nitrite reductase activity by incorporating a $ZnHis_3$ or $CuHis_3$ site, or that recapitulate the spectroscopic properties of unique electron-transfer sites in cupredoxins ($CuHis_2Cys$) or rubredoxins ($FeCys_4$). This work showcases the versatility of alpha helices as scaffolds for metalloprotein design and the progress that is possible through careful rational design. Our studies cover the invariance of carbonic anhydrase activity with different site positions and scaffolds, refinement of our cupredoxin models, and enhancement of nitrite reductase activity up to 1000-fold.

From the Contents

1. Introduction

Metalloproteins and peptides perform an immense number of the most critically important biochemical reactions required for all life.[1] Some of the most significant of these are the transfer of electrons within biological systems using redox-active metal centers and protein-supported metal-facilitated catalysis.[1c,2] Such significance highlights the extensive and wide range of metals in biological systems that can be tapped to aid in the development of de novo designed systems.

De novo protein design uses a bottom-up approach for the development of a functional protein in scaffolds completely different from native systems.[3] Such a strategy has two equally important and parallel goals. The first goal is that, through recapitulation of native metal binding sites in de novo scaffolds, which generally possess a significantly different secondary structure than the native system, we are challenging the accuracy and completeness of our understanding of the chemical principles and properties that govern the function of metalloproteins. This approach allows the basic requirements of the desired function to be studied, without the additional potentially convoluting "evolutionary baggage" that accompanies the study of native proteins.[4] The second goal is to generate novel catalysts that have improved properties for catalytic applications.[5] There are numerous approaches for the de novo design of a metalloprotein and an even larger number of designed scaffolds to work with.[6] There have been many reviews on the subject of metalloprotein design for catalysis,[3e] including an entire issue of *Accounts of Chemical Research*. Therefore, this Review highlights recent developments using purely alpha-helical structures, specifically using three-stranded coiled-coil peptides (3SCCs) and three helix bundle (3HB) proteins, emphasizing research from our group.

There are several advantages to 3SCCs and 3HB systems.[7] The TRI family of 3SCCs are designed based on CoilSer,[8] which itself originated from the polyheptapeptide designed by Hodges et al. to mimic coiled-coil tropomycin.[9] TRI consists of repeating heptads (*abcdefg*) with leucine residues in the first (*a* site) and fourth (*d* site) positions.[10] The other positions are helix-inducing (Ala, *c* sites), charged, and/or salt-bridging residues (Lys at *b*,*g* sites and Glu at *e*,*f* sites). The geometry of a super-coiled alpha helix, with 3.5 residues per turn aligns the leucine residues on one face of the alpha helix, thereby creating an amphiphilic structure. The crystallographic analogue or TRI, CoilSer (CS), is shown in Figure 1 A. In TRI, three alpha helixes associate in a parallel manner and the leucine residues pack together to form a hydrophobic core of *a* and *d* residues. Salt bridges between the *e* and *f* residues on neighboring strands

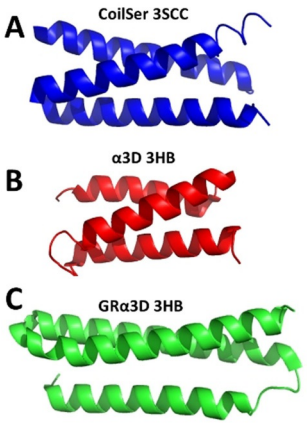

Figure 1. Structures of the peptide and protein scaffolds discussed in this Review: crystallographic TRI analogue CoilSer (A; PDB: 3PBJ[12]), α_3D (B; PDB: 2MTQ[13]), and GRα_3D (C; PDB: 6DS9[11]).

[*] Dr. T. B. J. Pinter, Dr. K. J. Koebke, Prof. V. L. Pecoraro
Department of Chemistry, University of Michigan
Ann Arbor, Michigan, 48109-1055 (USA)
E-mail: vlpec@umich.edu
The ORCID identification numbers for the authors of this article can be found under: https://doi.org/10.1002/anie.201907502.

stabilize the structure. To enhance the stability of the coiled-coil structures, the N-terminus and C-terminus are amidated and acylated, respectively. This arrangement creates layers of leucine residues in the structure's hydrophobic core that can be substituted by metal-binding residues to generate metal binding sites within the TRI scaffold. Table 1 lists the sequences of CS and TRI peptides that will be discussed in this Review.

Table 1: List of parent peptide sequences discussed in this Review.

Peptide[a]		*abcdefg*	*abcdefg*	*abcdefg*	*abcdefg*	
TRI	Ac–G	WKALEEK	LKALEEK	LKALEEK	LKALEEK	G–NH_2
CS	Ac–E	WEALEKK	LAALESK	LQALEKK	HEALEHG	–NH_2

Protein[b]	Loop	*abcdefg*	*abcdefg*	*abcdefg*	Loop
α_3D	MGS	WAEFKQR	LAAIKTR	LQAL	GGS
	EAE	LAAFEKE	IAAFESE	LQAY	KGKG

[a] N- and C-termini are acylated and amidated, respectively. [b] Produced recombinantly in *E. coli*.

Three parallel and independent strands must associate in the TRI/CS system to form a metal binding site. This differs significantly from most native metal binding sites, where the metal-chelating residues are all from the same strand. Therefore, a second scaffold was created that links the three alpha helixes together using flexible loops to create α_3D, an antiparallel 3HB protein (Figure 1B). However, the de novo design strategy remains the same as for TRI: substitution of hydrophobic core residues or residues near or on the flexible loops with metal-binding residues generates metal binding sites. An additional distinction between TRI and α_3D is that since TRI is formed by the association of three identical strands, only symmetric metal binding sites can be generated. In α_3D, however, each amino acid can be independently mutated, thereby allowing complete control over the residues around and within the metal coordination sphere. Finally, to increase the stability of the 3HB scaffold on increasing the number of destabilizing mutations in the parent scaffold α_3D, we designed a lengthened version called Grand α_3D (GRα_3D, Figure 1C).[11] In this Review, we will describe advances that we have made towards the rational design of both catalytic and electron-transfer metal binding sites within our TRI (including TRI, GRAND, and CoilSer peptides) and α_3D scaffolds (including α_3D and Grand α_3D).

2. De Novo Designed Metallopeptides for Catalysis

Metals catalyze an extremely diverse set of reactions in biological systems.[14] The same metal in different peptidic environments can possess wildly variant activities and display disparate reactions. Iron, for example, plays critical roles in oxygen storage and transport, electron transfer, and numerous hydroxylation, dioxygenation, oxidation, and hydrolysis reactions; each reaction is modulated only by the specific environment in which the metal is located.[15] Thus, by approximate recreation of the positions of specific conserved residues that surround native metal binding sites, we are able to generate desired catalytic activities in our de novo scaffolds. There are three functions that we have had the most success with to date, zinc-catalyzed hydrolysis, nitrite reductase activities, and electron-transfer sites.

Tyler B. J. Pinter received his PhD from the University of Western Ontario (London, Ontario, Canada) working with Prof. Martin Stillman, where he studied the metal-binding properties of metallothionein by electrospray ionization mass spectrometry. He is currently an NSERC-funded research fellow working with Prof. Vincent Pecoraro on developing de novo designed models of metal binding sites.

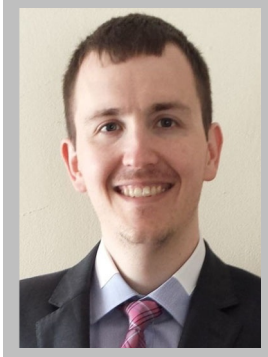

Karl J. Koebke obtained his PhD from the University of Wisconsin–Milwaukee (USA) working with Prof. Andy Pacheco on the kinetics of nitric oxide dioxygenation in heme proteins. He then carried out postdoctoral research for three years with Prof. Vincent Pecoraro, where he designed a plethora of de novo constructs including nitrite reductase and cupredoxin mimics. After a year working with Prof. Timothy Stemmler (Wayne State University) on mitochondrial FeS cluster biogenesis, he is now working with Prof. Neil Marsh (University of Michigan) on self-assembling protein nanocages.

Vincent L. Pecoraro is the John T. Groves Collegiate Professor of Chemistry at the University of Michigan, Ann Arbor (USA). He is an expert in bioinorganic and supramolecular chemistry, having made substantive contributions to the understanding of photosynthetic water oxidation and vanadium biochemistry. In recent years he has been a leader in the field of metalloprotein design and the development of metallacrowns as biomolecular imaging agents. He served as an Associate Editor for Inorganic Chemistry for over 20 years and is a fellow of both the ACS and AAAS.

2.1. Development of Zinc Sites as Models of Carbonic Anhydrase Hydrolytic Activity

Building upon our wealth of knowledge on the binding of heavy metals to tris(cysteine) layers in our de novo designed scaffolds,[16] we turned our attention to the more complex problem of recreating catalytic metal sites. This is arguably a more ambitious goal, as the design of the metal binding site must not only include the primary coordinating ligands but support access of the substrate for efficient catalysis.

As a first attempt at inserting a catalytically active metal into our scaffolds, we targeted the symmetric tris(histidine) environment of carbonic anhydrase (CA). CA catalyzes the reversible hydration of CO_2 (Reaction (1)), and is critical to buffering the pH value of blood and respiration. Native CA represented a good first target because of the relative simplicity of the metal binding environment as well as its high catalytic activity.[17] Mutating two different leucine layers in the TRI scaffold at each end of the coiled-coil, one with cysteine near the N-terminus and the other with histidine near the C-terminus, gives TRIL9CL23H. Crystallographically, the tris(cysteine) site was shown to bind a Hg^{II} ion for structural stability, while the tris(histidine) site supported a zinc ion for catalysis.[12]

$$HCO_3^- + H^+ \rightleftharpoons CO_2 + H_2O \quad (1)$$

The inclusion of two layers of metal binding residues destabilized the structure compared to the parent TRI system, but the inclusion of the heavy-metal binding site improved the stability beyond that of the nonmutated form. The structural site was shown to increase the stability of the 3SCC significantly through formation of a trigonal Hg^{II}-Cys_3 structure. A comparison of the crystal structures showed the zinc active site had an extremely similar geometry to that of native CA, including an exogenous water molecule or hydroxide coordinated to the zinc ion, although the orientation of the coordinating imidazole rings differs between the two (Figure 2).

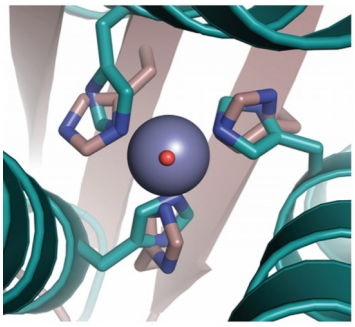

Figure 2. Overlay of the $Zn^{II}N_3O$ site in $[Hg^{II}]_S[Zn^{II}(H_2O)]_N$ $(CSL9PenL23H)_3$ with the active site of human CAII. CS is shown in cyan (PDB: 3PBJ[12]) and CAII in beige (PDB: 2CBA[17]). The solvent molecule associated with CS is shown in red and that associated with CAII lies below the zinc ion. Reprinted from Ref. [12] with permission. Copyright 2012 Nature Publishing Group.

We examined the activity of $[Hg^{II}]_S[Zn^{II}]_N$TRIL9CL23H (subscripts denote metal-coordinating protein ligands: HgS_3 and ZnN_3) for the hydrolysis of *p*-nitrophenyl acetate (pNPA) and hydration of CO_2. The hydrolysis of pNPA is well-studied as a result of the ease of monitoring the formation of the colored *p*-nitrophenolate. Our CA model $[Hg^{II}]_S$-$[Zn^{II}]_N$TRIL9CL23H showed a pH-dependent activity (Figure 3, pK_a of hydrolysis ca. 8.8), with a maximum k_{cat}/K_M value within 100-fold of that of CAII (the isoform with the highest pNPA activity) at pH 9.5. Table 2 compares the activities of our model scaffolds for pNPA hydrolysis. Notably, our CA mimic did not exhibit product inhibition under our conditions, a common issue with small-molecule CA models.[18]

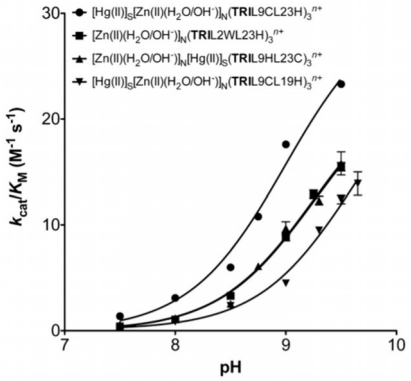

Figure 3. pH-dependence of the catalytic efficiency for pNPA hydrolysis by Zn^{II}-bound TRI peptides: $[Hg^{II}]_S[Zn^{II}]_N$-TRIL9CL23H (●), $[Zn^{II}]_N$-TRIL2WL23H (■), $[Zn^{II}]_N[Hg^{II}]_S$- TRIL9HL23C (▲), and $[Hg^{II}]_S[Zn^{II}]_N$-TRIL9CL19H (▼). Reprinted from Ref. [12] with permission. Copyright 2013 American Chemical Society.

Table 2: Kinetic parameters of pNPA hydrolysis by Zn-TRI peptides.

Peptide scaffold	pK_a	k_{cat}/K_M (max) [$M^{-1}s^{-1}$][a]	k_{cat} (max) [s^{-1}]
$[Zn]_N$(TRIL2WL23H)	9.2	25	0.055
$[Hg]_S[Zn]_N$(TRIL9CL23H)	9.0	31	0.053
$[Zn]_N[Hg]_S$(TRIL9HL23C)	9.2	24	0.030
$[Hg]_S[Zn]_N$(TRIL9CL19H)	9.6	27	0.076

[a] Determined by fitting the pH-dependent k_{cat}/K_M versus pH data.

Significantly, this model lacks an important secondary sphere interaction, which plays a significant role in enhancing the rate of CO_2 hydration in CAII. T199A mutants of CAII remove a hydrogen-bond acceptor that has been shown to activate the zinc-coordinated water molecule in the mechanism of hydrolysis,[19] thereby reducing the activity approximately 100-fold versus that of the native enzyme and falling to comparable rates as our CA model. As our $[Hg^{II}]_S$-$[Zn^{II}]_N$TRIL9CL23H only reproduced the primary coordination sphere, we had essentially mimicked the activity of CAII T199A.

When we examined the rate constants of the CO_2 hydration activity, the native reaction of CAII, $[Hg^{II}]_S$-$[Zn^{II}]_N$TRIL9CL23H showed rates within 500-fold of the native enzyme at pH 9.5, outperforming the best small-

Table 3: Kinetic parameters of CO_2 hydration by enzymes, small molecules, and our model scaffolds.

Enzyme/ Model	pK_a	pH	k_{cat} [s^{-1}]	K_M [mM]	k_{cat}/K_M [$L\,mol^{-1}\,s^{-1}$]	k_2 [$L\,mol^{-1}\,s^{-1}$]	Ref.
CAII	6.8[a]	8.8	8.2×10^5	8.9	9.2×10^7		[25]
CAIII	8.5	9.0	8×10^3	20	4×10^5		[26]
TRIL9CL23H	8.82[b]	9.5	1.8×10^3	10.0	1.8×10^5		[12]
α_3DH3	9.4	9.5	1.3×10^2	3.5	3.8×10^4		[24]
Zn^{II}([14]aneN4)	9.8					5040[c]	[27]
Zn^{II}([12]aneN4)	8.1					3012	[18a]
Zn^{II}(nitrilotris(2-benzimidazolylmethyl-6-sulfonate)	8.3					2180	[28]
Zn^{II}(tris(4,5-di-*n*-propyl-2-imidazolyl)phosphine)	8.0					2480	[29]

[a] Taken from Ref. [30]. [b] pK_a of pNPA hydrolysis. [c] pH-independent second-order rate constant (maximal rate) calculated using pK_a = 9.8 and the measured rate of 690 $M^{-1}s^{-1}$ at pH 9.0.

molecule CA model by over 70-fold (Table 3). Since our study was reported, models with higher pNPA activities have been described, such as MID1, which showed a maximum k_{cat}/K_M of 660 $M^{-1}s^{-1}$ at pH 9.[20] To date, $[Hg^{II}]_S[Zn^{II}]_N$TRIL9CL23H retains the title of the model with the highest CO_2 hydration activity. This study was a keystone work, showing what could be achieved with our de novo scaffolds that reproduce only the first coordination sphere.

2.2. Impact of the Position of the Zinc Binding Site on the Hydrolytic Activity

There is the possibility that the presence of the second metal site $[Hg^{II}]_S$ enhanced the activity of our CA model by altering the fraying or "breathing" of the individual strands of the 3SCC. We therefore examined models that lacked the stabilizing tris(cysteine) heavy-metal binding site.[21] When the Cys layer was removed, TRIL23H denaturation studies demonstrated that the 3SCC was less stable, although the zinc affinity was unaffected. The activity of this model to pNPA was nearly identical to that of $[Hg^{II}]_S[Zn^{II}]_N$TRIL9CL23H except at high pH values, which we attributed to decreased stability caused by the loss of the stabilizing $[Hg^{II}]_S$ site under more basic conditions.

To determine whether the specific location of the metal binding site plays a significant role in the resulting activity, we next designed CA models that modified the position of the zinc site within the leucine-layered core of our 3SCC design. For example, the orientation of the coordinating histidine residues and the resulting placement of the zinc ion has the potential to significantly influence both solvent and substrate access, as well as hydrogen-bonding interactions—factors known to play significant roles in the activity of native CAs.[22] Our scaffolds offer a significant advantage over designing metal binding sites in native or more complex scaffolds as the inclusion of the metal binding site a) does not significantly alter the scaffold geometry, b) can be moved to different positions in the 3SCC by simply changing the location of leucine substitutions, and c) can be placed in a number of approximately geometrically equivalent positions along the 3SCC as a result of the presence of multiple leucine layers.

We developed the inverted complement to $[Hg^{II}]_S[Zn^{II}]_N$TRIL9CL23H—$[Hg^{II}]_S[Zn^{II}]_N$TRIL9HL23C—by placing the zinc active site towards the N-terminus.[21] This construct has a 10-fold lower zinc affinity than TRIL9CL23H and TRIWL23H at pH 7.5 and a 4-fold weaker activity at pH 9, thus highlighting the importance of the position and orientation of the metal site in the de novo scaffolds. Kinetic analysis of pNPA hydrolysis under Michaelis–Menton conditions showed the inverted construct had a reduced k_{cat} value of 0.020 s^{-1} at pH 9.5 (half that of TRIL9CL23H). This decrease in k_{cat} was, in part, counteracted by a smaller K_M value so k_{cat}/K_M only decreased from 23.3 to 15.8 $M^{-1}s^{-1}$ (Table 2).

Earlier, we had shown that the position of the heavy-metal binding tris(thiolate) site possessed different properties if it were placed at the *a* site versus a *d* site within the heptad; for example, the pK_a value, coordination number, and ligand positions change for cadmium and mercury in these sites.[23] Hypothesizing a similar effect could exist for zinc in tris(histidine) sites, TRIWL9CL19H was studied. This construct showed a fivefold decreased affinity for zinc and an increased pK_a value for pNPA hydrolysis of 9.6 (from 9.2 in TRIL9CL23H; Figure 3). The construct also showed comparable pNPA hydrolysis rates with k_{cat}/K_M values similar to those of TRIL9CL23H and TRIL9HL23C, but with an increase in the K_M value to 2.8 mM. These results demonstrate the potential to tune the K_M and pK_a values by repositioning the metal binding site, with the catalysis largely unaffected. The location of the metal site in a de novo designed scaffold should be based on the ease of incorporating secondary sphere interactions that enhance the reaction rate.

2.3. Development of a Hydrolytic Zinc 3HB Protein

The intrinsic symmetry of our self-assembling 3SCC scaffold has numerous benefits, as already discussed above. However, to design a functional hydrogen-bonding network and to model the asymmetry in the second coordination sphere of CAII, we next designed a model of CA in our α_3D-type scaffold.[24] Replacement of three of the core leucine layers on the C-terminal side of the original α_3D along with a H72V mutation to remove any possible unintended zinc coordination gave α_3DH3. Zinc binds tighter to this three-helix bundle peptide than any 3SCC model, with an apparent K_d = 0.15 μM at pH 7.5 and 0.06 μM at pH 9 (TRIL9CL23H: K_d = 0.8 μM at pH 7 and 0.22 μM at pH 9). Extended X-ray absorption fluorescence spectroscopy showed the zinc coor-

dination sphere consisted of three zinc histidine scatterers at a distance of 1.99 Å and one zinc-oxygen scatterer at a distance of 1.90 Å. These parameters are nearly identical to those of the native CAII.

As with the TRI 3SCC, the CO_2 hydration activity of α_3DH3 showed a pH-dependence. The reaction was analyzed between pH 8 and 9.5, and showed a maximal efficiency at higher pH, $k_{cat}/K_M = 69000\,M^{-1}s^{-1}$. The catalytic p$K_a$ value was 9.4, compared to 8.8 for the 3SCC model. The maximum measured k_{cat}/K_M value was $38000\,M^{-1}s^{-1}$, which is 14-times faster than the best small-molecule model, but 2.5-times slower than the best TRI 3SCC model, TRIL9CL23H. Again, this model did not display any product inhibition, a significant advantage over small-molecule studies to date. Compared to the native enzyme, α_3DH3 falls within 2400-fold of the fastest isozyme, CAII (Table 3).

2.4. Zinc-Catalyzed Hydrolytic Activity in Other Helical Scaffolds

As mentioned above, other research groups have developed different helical scaffolds that bind zinc ions and have been shown to possess zinc-catalyzed hydrolytic activity. The Kuhlman group developed a zinc-mediated homodimer in a helix-turn-helix motif. The design of the homodimer contains two four-coordinate zinc ions, each supported by a His_3O binding site. A fourth His ligand (intended as a fourth primary coordinating ligand) creates a small-molecule binding pocket. As with our current generation of CA models, no second-sphere interactions were intentionally designed. MID1-Zn showed an improved hydrolysis of pNPA compared to our TRI scaffold, with a k_{cat}/K_M of $660\,M^{-1}s^{-1}$ at pH 9, which was attributed to the active site cleft being more accessible in the homodimer. Recently, this group described the artificial evolution of the MID1 catalyst, improving upon the hydrolysis of a racemic fluorogenic ester 70000-fold.[31] A designed metallo-β-lactamase was described by the Tezcan group that consisted of a tetramer of modified cytochrome cb562, Zn_8:$AB3_4$.[32] The design of this scaffold relies on a zinc-mediated self-assembling interface, such that four of the eight zinc ions have a purely structural role, while the remaining four are catalytically active. This protein, in addition to conferring the metallo-β-lactamase activity, also showed good activity towards pNPA, with k_{cat}/K_M of $32\,M^{-1}s^{-1}$ at pH 9. In a similar approach, the Korendovych group showed how short peptides could self-assemble, facilitated by zinc binding to His residues, to form zinc-mediated amyloid fibrils with esterase activity.[33] These zinc-binding amyloid fibrils, which consist of beta sheets rather than alpha helices, can catalyze ester hydrolysis, with a $k_{cat}/K_M \approx 150\,M^{-1}s^{-1}$ at pH 9 and a maximal $k_{cat}/K_M = 360\,M^{-1}s^{-1}$ at pH 10.3.

3. Development of Copper Centers as Models of Nitrite Reductase Activity

The de novo design of redox-active metalloenzymes is more complicated than that of redox-inactive metal centers, such as the zinc-containing models of CA. The change in the oxidation state of the metal will not only modify the overall electrostatic charge of the binding site, but, generally speaking, different oxidation states possess differing ligand environments and geometric preferences. Cu^I, for example, shows a stronger preference for softer ligands and a lower coordination number than Cu^{II}. Therefore, the de novo design of redox-active metalloenzymes must consider the coordination environment of both the reduced and oxidized species, in addition to the criteria described above for redox-inactive metals. Fortuitously, our de novo scaffolds offer some significant advantages over small-molecule models, as the geometry of the metal binding site is constrained by the stable folding of the scaffold in the absence of a metal. Additionally, only small reorganizations have been observed upon metal binding to our scaffolds, and are dependent on the location of the site within the scaffold and on the metal being examined.[34] As mentioned above, most of the current small-molecule mimics are only soluble in organic solvents and optimized to bind a single oxidation state of copper. Thus, our scaffolds are well-suited to model redox-active metalloenzymes.

Recently, we have described several advances in the development of models with copper nitrite reductase (CuNiR) activity. CuNiRs catalyze the reduction of nitrite to nitric oxide through Reaction 2, the second step in the dissimilatory pathway of nitrate to dinitrogen. CuNiR is a homotrimeric copper enzyme that possesses two copper binding sites, a type 1 electron-transfer copper center Cu-(His_2)(Cys)(Met), and a type 2 catalytic copper center Cu-(His_3)(OH_2). The catalytic type 2 copper center exists in a distorted tetrahedral environment, intermediate to the preference of the cuprous and cupric species so as to minimize the reorganization energy of the protein in response to changes in the oxidation state.[35] The mechanism of nitrite reduction is well-studied; briefly, nitrite binds to the type 2 catalytic site first, followed by gated electron transfer from the reduced type 1 site to the type 2 site. Proton-coupled electron transfer, facilitated by hydrogen bonding between a histidine (H225) and an aspartate (E98) to water and the bound substrate, facilitate the catalysis.[36] These residues have been shown to be critical for the high activity of native CuNiRs with at least a 100-fold decrease in activity upon their removal.

$$NO_2^- + e^- + 2\,H^+ \rightleftharpoons NO + H_2O \quad (2)$$

3.1. First Generation CuNiR Models

Noting that the geometry of the zinc site in our CA model $Hg^{II}_S Zn^{II}_N(TRIL9CL23H)_3$ was very similar to that of the type 2 Cu center in CuNiR, we first looked at the binding of copper in the tris(histidine) site of TRI 3SCC using the simplified TRIL23H, which lacks the heavy-metal binding tris(cysteine) site.[37] An overlay of the zinc site in $Hg^{II}_S Zn^{II}_N(TRIL9CL23H)_3$ with the copper centers of CuNiRs showed similar ligand geometries, each coordinating the metal through the ε-nitrogen atom of the histidine and with a coordinated water ligand (Figure 4). The charge and Lewis acidity of Zn^{II} resembles that of Cu^{II}, and the d^{10}

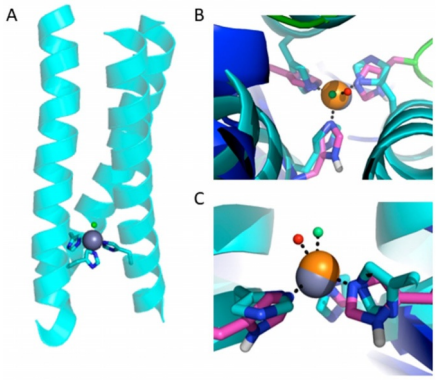

Figure 4. A) Model of Cu-TRIL23H based on the structure of $Hg^{II}_{S}Zn^{II}_{N}$CSL9CL23H. B) View of the $Zn^{II}(H_2O)(His)_3$ site along the pseudo-threefold axis (light gray), superimposed on the type 2 $Cu^{II}(H_2O)(His)_3$ site in NiR from *R. sphaeroides* (PDB: 2DY2; dark gray). Coordinated water molecules are shown as spheres. C) Side view of the two metal sites, as in (B). Reprinted and adapted from Ref. [37] with permission. Copyright 2012 Proceedings of the National Academy of Sciences of the United States of America.

configuration mimics the electron configuration of Cu^I. Therefore, we were confident that this peptide would be a suitable model of the type 2 site of CuNiR, thus allowing the reaction to be studied in an aqueous environment using the native ligands, unlike small-molecule models, while removing the convolution of the two copper sites in the native CuNiR.

The binding of Cu^I to the histidine sites was confirmed using ^{1}H NMR spectroscopy.[37] The metal-free apo-TRIL23H showed two singlets in the aromatic region of the ^{1}H NMR spectrum, at $\delta \approx 7.7$ and 7.0 ppm, which corresponds to the protons on the ε- and δ- nitrogen atoms, respectively. Upon addition of 1 equiv of Cu^I, these singlets gave rise to multiple signals, thus indicating the copper bound specifically to the histidine residues. Additionally, pH titrations on Cu-TRIL23H monitored by ^{1}H NMR spectroscopy showed the presence of free imidazole protons, consistent with $Cu^I(His_3)$, only below pH 4.45. Further characterization using XAS revealed that the 1s→4p pre-edge feature, the intensity of which can be diagnostic of the coordination number of the copper species,[38] was also consistent with a three-coordinate Cu^I ion. The EXAFS data for Cu^ITRIL23H were best fit by three N/O scatterers at a distance of 1.93 Å with additional backscattering at longer distances, characteristic of histidine coordination. The unusually large Debye–Waller factors of these His scatterers suggested a distorted trigonal-planar geometry. The dissociation constant K_d for Cu^I was determined by competitive titration with bathocuproine disulfonate (BCS^{2-}) to be 3.1 pM at pH 5.9 and 0.2 pM at pH 7.5.

Cu^{II} binding was investigated by UV/Vis spectroscopy, with a broad absorption observed around 640 nm ($\varepsilon = 135\,M^{-1}cm^{-1}$), consistent with a $Cu^{II}(His)_3$ site containing either one or two exogenous water ligands.[39] The EPR spectrum of Cu^{II}TRIL23H was consistent with a five-coordinate type 2 copper center $[Cu^{II}(His)_3(H_2O)_2]$. The addition of nitrite to Cu^{II}TRIL23H resulted in a decrease in the $A_{\parallel}$ mode (the z-axis hyperfine coupling constant) by 9 Gauss, which is indicative of nitrite binding directly to the copper center, as previously shown for native NiR.[40] The K_d value for Cu^{II} of this model was determined by quenching Trp fluorescence to be 40 nM at pH 5.9 and 8.7 nM at pH 7.5.

It is possible to calculate the reduction potential of the Cu^I/Cu^{II} couple from the affinities for Cu^I and Cu^{II} using the Nernst equation. The reduction potential for this model is 400 mV at pH 5.9 and 430 mV at pH 7.5, much higher than is typical for type 2 copper centers,[41] and actually falling closer to those reported for type 1 copper centers. This could be due to the trigonal geometry of the Cu^I state being stabilized in the highly symmetric $(His)_3$ binding site, thereby raising the reduction potential. Despite this elevated reduction potential, we examined the NiR activity of CuTRIL23H. This model was shown to be capable of generating NO from nitrite, by capture of the produced NO to form the colored FeEDTA-(NO).[42] FTIR-GC analysis of the headspace showed no detectable amounts of N_2O, which is a common by-product in other NiR model systems, and represents a significant success with our de novo approach.

Using ascorbate as a sacrificial electron donor, whose signal can be conveniently followed in the UV region at 265 nm to monitor the reaction, we assayed for NiR activity under catalytic conditions and determined a maximum first-order rate constant of $4.6 \times 10^{-4}\,s^{-1}$ at pH 5.8. A significant decrease in the reaction rate as a function of increasing pH value is likely caused by changes in the Cu^IHis_3 coordination environment or the involvement of protons in the nitrite reduction reaction. Although this catalytic rate represents only a modest rate compared to that of the native CuNiR, this model was the only example of a stable, functional $Cu(His)_3$ site in aqueous solution capable of multiple turnovers with no observed decrease in efficiency.

3.2. Probing the Cu Site

It is exceptional that our first generation de novo enzymes possess good activities in the absence of any modeling beyond that of the primary metal coordination sphere. Thus, to improve on the CuNiR activity, it was clear that optimization would largely depend on the effect of modifications to the second coordination sphere as well as the electrostatic environment surrounding the copper binding site.[43] Changes to the reaction's free energy barrier ($\Delta G^{\ddagger}$), which would result in modification of the enzymatic rates, can be brought about by changes to the electrostatic environment of the active site, through stabilization of charge density in the transition state. Dynamic aspects of enzyme active sites, that is the pico- to microsecond or longer vibrational and translational motions inside and around the catalytic site, are also involved in determining the overall reaction rates. The dynamics and electrostatic factors that drive catalysis can be studied using vibrational probes of enzyme active sites.[44] These studies provide details on the flexibility of the active site, which determines how the substrate accesses the active site and the product is transported away, as well as changes in the reaction barrier with respect to the molecular dynamics around the active site.[45]

In collaboration with the Kubarych group, we studied the copper environment within our CuNiR model by examining the ultrafast dynamics of carbon monoxide bound to CuTRI-H as a vibrational probe of the $Cu(His)_3$ environment.[46] We used two-dimensional IR spectroscopy as an in situ probe of the active site to further connect our understanding of our de novo constructs with that of small-molecule models.[47] The 2D-IR spectrum showed two bands that correspond to the excitation of the ground-state ($\nu = 0 \rightarrow 1$, 2063 cm^{-1}) and excitation of the first excited-state ($\nu = 1 \rightarrow 2$, red-shifted to 2039 cm^{-1} due to CO vibrational anharmoncity) transitions. Following vibrational excitation, we observed a time-dependent anharmonicity in the vibrational modes of the bound CO, with a decay constant of 2 ps. The frequency shift brings the two bands closer together, as the ν_{01} transition red-shifts and the ν_{12} transition blue-shifts. The magnitude of the excited-state blue-shift exceeded that of the ground-state red-shift. We also investigated the modified peptide (TRI-H K22Q K24Q), in which six positively charged lysine residues near the copper site are replaced by neutral glutamine groups. This protein exhibited similar anharmonicity as the vibrational transition, thus suggesting that this feature is reproducible in other sequences and is likely common to our other 3SCC scaffolds.

Computer modeling calculations on the full de novo protein were performed to understand the steric and electrostatic interactions that give rise to this behavior. By using a QM/MM ONIOM approach, with the Cu, imidazole ligands, and CO adduct in the QM (B3LYP/6-311G(d,p)) layer, we observed a $>6°$ decrease in the Cu-C–O bond angle of the vibrational excited state. This bending is consistent with the picosecond dynamics observed in the vibrational frequency shifting dynamics and supports that the peptide enhances coupling to the CO stretch. This result highlights the role of the peptidic environment and is one of the significant advantages of our de novo approach. Further calculations showed that the electric field from the parallel 3SSC peptide scaffold distorts the geometry of the copper-coordinating histidine ligands and is responsible for the Cu-C-O bend coupling to the CO excited-state stretch, rather than directly affecting the carbonyl group. This coupling to the excited-state bend was strongly dependent on the orientation of the histidine coordination to the copper center, likely a result of the position of the dipole moments (ca. 3.6 D) from each of the individual His ligands (Figure 5). These calculations reveal the role of electrostatics in tuning the molecular dynamics and the energy landscape of ligand coordination within our $Cu(His)_3$ site. Thus, by modification of the electrostatic environment, either by changing the location within the 3SCC (coiled-coil dipole) or by positioning of charged residues in proximity to the site, it is possible to improve our CuNiR.

To improve on this modest CuNiR activity, we then considered the role of the electrostatic environment surrounding the copper binding site first by modification of outer-sphere residues that change the electrostatic environment of the copper center (Figure 6A), followed by changes to inner-sphere residues (Figure 6B).

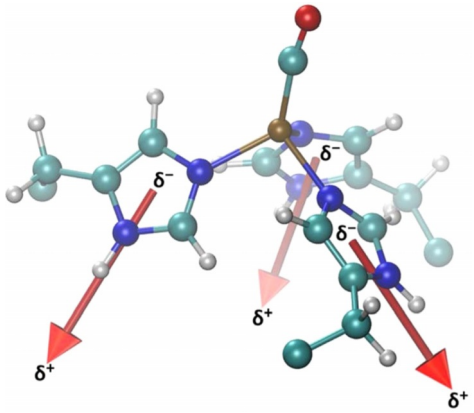

Figure 5. Dipole moment of each histidine ring in Cu^{I} (TRIL2WL23H)3-(CO) + with an average magnitude of 3.6 D. These dipolar side chains are able to couple to the electrostatic environment produced by the protein scaffold. Reprinted from Ref. [46] with permission. Copyright 2013 American Chemical Society.

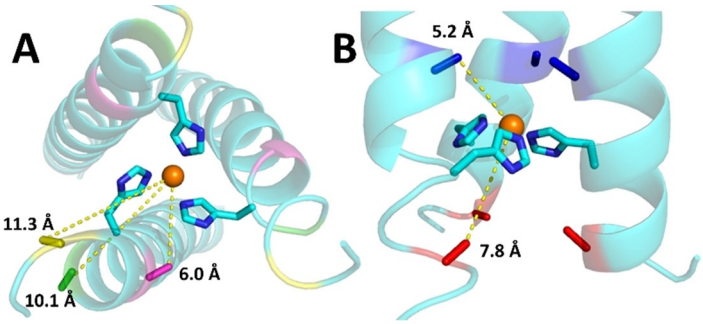

Figure 6. Model of CuNiR highlighting the location of A) outer-sphere and B) inner-sphere residue substitutions near the Cu binding site of TRI-H based on the crystal structure of $Zn^{II}_{N}Hg^{II}_{S}$(CSL9PenL23H)$_3$ (PDB: 3PBJ). The copper atom is shown as an orange sphere, distances to the β-carbon atom of the residues being substituted are indicated for outer-sphere substitutions—K22 (magenta), E24 (green), and K27 (yellow)—and inner sphere—L19 (blue), and L26 (red).

3.3. Modification of the Charge Density Around the Copper Binding Site

Modification of the charge density around a redox-active metal binding site (by substituting residues of different charges) will have significant effects on the stability and structure of the different oxidation states, and thus the redox potential, and ultimately the catalytic efficiency or mechanism of redox-active metalloenzyme sites.[48] For example, the protein peptidylglycine α-hydroxylating monooxygenase (PHM) has a (His_3) active site structurally similar to CuNiR, but plays a role in electron transfer instead of being directly involved in catalysis, as is the case for CuNiR.[49] Historically, these studies were performed on native proteins, which bring along the complexity and convoluting factors of native systems. Therefore, we sought to examine the role of the electrostatic environment around the Cu center in our de novo CuNiR 3SCC model TRI-H by modifying the charge of nearby residues. We designed and synthesized several

Table 4: Peptide sequences of outer-sphere (upper), inner-sphere (middle), and primary coordinating (lower) residue substitutions for CuNiR activity studies. The position of these modifications can be viewed in Figure 6.

Peptide[a]		*abcdefg*	*abcdefg*	*abcdefg*	*abcdefg*		Δ_{charge}
TRI-H	Ac–G	WKALEEK	LKALEEK	LKALEEK	HKALEEK	G–NH_2	
TRI-HK22Q	Ac–G	WKALEEK	LKALEEK	LKALEEQ	HKALEEK	G–NH_2	−3
TRI-EH	Ac–G	WKALEEK	LKALEEK	LKALEEE	HKALEEK	G–NH_2	−6
TRI-EHE27K	Ac–G	WKALEEK	LKALEEK	LKALEEE	HKAKEEK	G–NH_2	0
TRI-EHE27Q	Ac–G	WKALEEK	LKALEEK	LKALEEE	HKAQEEK	G–NH_2	−3
TRI-EHK24Q	Ac–G	WKALEEK	LKALEEK	LKALEEE	HQALEEK	G–NH_2	−9
TRI-EHK24E	Ac–G	WKALEEK	LKALEEK	LKALEEE	HEALEEK	G–NH_2	−12
L19I	Ac–G	WKALEEK	LKALEEK	LKAIEEK	HKALEEK	G–NH_2	0
$L19_DL$	Ac–G	WKALEEK	LKALEEK	LKA_DLEEK	HKALEEK	G–NH_2	0
L19A	Ac–G	WKALEEK	LKALEEK	LKAAEEK	HKALEEK	G–NH_2	0
L26A	Ac–G	WKALEEK	LKALEEK	LKALEEK	HKAAEEK	G–NH_2	0
L19D	Ac–G	WKALEEK	LKALEEK	LKADEEK	HKALEEK	G–NH_2	−3
L26D	Ac–G	WKALEEK	LKALEEK	LKALEEK	HKADEEK	G–NH_2	−3
TRI-$_{\delta m}$H	Ac–G	WKALEEK	LKALEEK	LKALEEK	$_{\delta m}$HKALEEK	G–NH_2	0
TRI-$_{\varepsilon m}$H	Ac–G	WKALEEK	LKALEEK	LKALEEK	$_{\varepsilon m}$HKALEEK	G–NH_2	0
TRI-$_{\varepsilon m}$H L19A	Ac–G	WKALEEK	LKALEEK	LKAAEEK	$_{\varepsilon m}$HKALEEK	G–NH_2	0

[a] The N- and C-termini are acylated and amidated, respectively.

modified peptides with substituted residues, as listed in Table 4 (top), located neither within the hydrophobic interior of the 3SCC (which could lead to significant destabilization) nor directly involved in Cu coordination (Figure 6 A).[50]

The effect of the pH value on the binding of copper to the outer-sphere-modified peptides was followed using UV/Vis spectroscopy. At a near-neutral pH value, Cu^{II}-TRI-H shows a broad band centered at 644 nm, assigned as the d-d transition of the copper atom in the His_3 environment. The pH profiles of the binding of copper to TRI-H are complicated by multiple competing and overlapping processes that occur as a function of the pH value. The most significant process is the formation of 3SCC, which is known to occur around the pK_a value of glutamate residues involved in salt bridging at *e*-sites (the fifth position in the heptad repeat) around pH 4.5. Other processes are dependent on the protonation state, charge, and copper-binding propensity of the imidazole ligand (pH 5.5–8), as well as the protonation state of any coordinated water molecules (pH > 8). Thus, there are two major changes in the UV/Vis spectrum as a function of the pH value: a transition associated with 3SCC formation and copper binding to the $(His)_3$ site at low pH values, which is complete by approximately pH 5, and the deprotonation of the water coordinated to the copper to form a hydroxide with a $pK_a \approx 8.5$ (Figure 7). Other outer-sphere modifications with different charges showed similar pH profiles for the binding of copper at lower pH values, but distinctly different profiles at higher pH values as a result of the various pH effects coming in to play. TRI-EH, for example, showed a significantly more basic water deprotonation step (pK_a 9.86). XAS measurements of the cuprous forms and EPR measurements on the cupric forms of TRI-H and TRI-EH showed no significant difference in the geometry of the copper site between the two scaffolds at pH 5.8. Minor differences in the intensity of the Cu^I pre-edge feature and lower Debye–Waller values of the Cu-N scatterers in the EXAFS region suggest a slightly more symmetric trigonal-planar geometry for the TRI-EH versus a more distorted T-shaped geometry for the parent TRI-H.

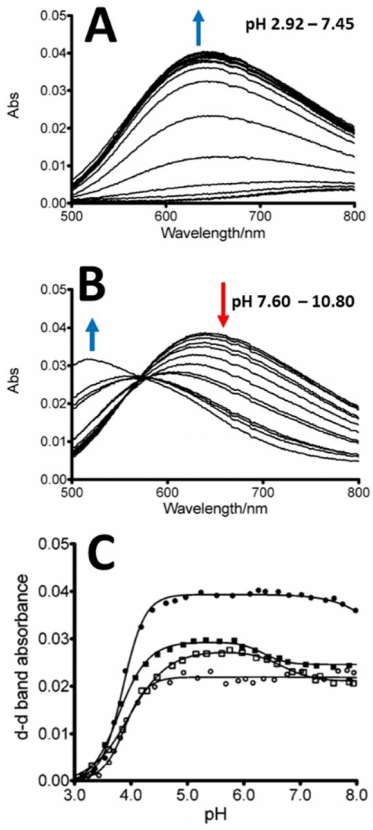

Figure 7. pH titration of $Cu^{II}(TRI\text{-}H)_3$ A) below and B) above pH 7.5. C) Changes in the absorbance of the Cu^{II} d-d band when Cu^{II} was bound to TRI-H (●; Δcharge = 0); TRI-EHE27K (○; Δcharge = 0); TRI-EH (■; Δcharge = −6); and TRI-EHK24E (□; Δcharge = −12). Reprinted and adapted from Ref. [50] with permission. Copyright 2013 American Chemical Society.

Dissociation constants for the Cu^{I} and Cu^{II} states of the models were measured for the series of models with outer-sphere modifications. The K_d value for Cu^{I} was found to decrease by over two orders of magnitude as the charge was decreased from 0 to −12, while the K_d value for the Cu^{II} species with the same modifications only showed a modest decrease in affinity. These values were then used to calculate the reduction potentials, using the Nernst equation, and plotted as a function of the charge difference from the parent TRI-H (Figure 8A) at two specified pH values. These values

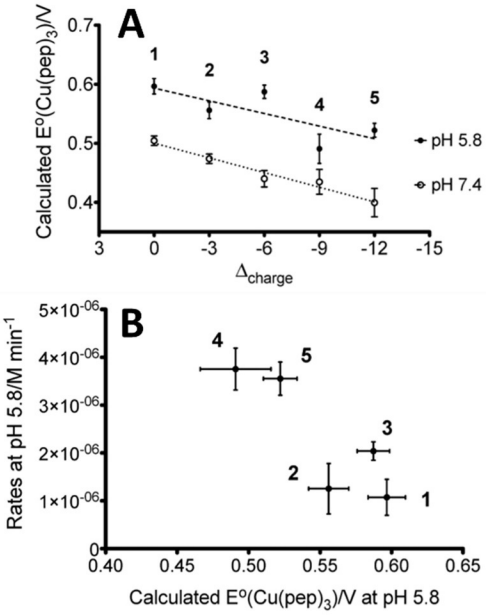

Figure 8. A) Calculated reduction potentials in relation to the changes in the local charge at pH 5.8 and pH 7.4. B) Rates of NiR activity versus calculated reduction potentials at pH 5.8. Peptides: 1) TRI-EHE27K, 2) TRI-EHE27Q, 3) TRI-EH, 4) TRI-EHK24Q, 5) TRI-EHK24E. Reprinted and adapted from Ref. [50] with permission. Copyright 2013 American Chemical Society.

also show a linear decrease as a function of increasing negative charge at both pH 5.8 and 7.5 with a slope of 100 mV per 1.6 pH units, which is consistent with one proton per electron. This decrease in the calculated reduction potential is more reflective of the destabilization of the cuprous species in a more negatively charged environment than the stabilization of the cupric form, thereby resulting in a less positive reduction potential. The differences in the affinities of the cupric and cuprous forms of each model are separated by approximately 100 mV, with the more acidic pH values giving the more positive reduction potentials.

We had originally designed the series of outer-sphere CuNiR models with increasing negative charge to stabilize the more positively charged Cu^{II} species, which would, in turn, decrease the reduction potentials. Although we did indeed observe the expected decrease in the reduction potential across the series, it was due to the destabilization of the Cu^{I} species rather than the stabilization of the Cu^{II} species. Thus, the finding that the Cu^{I} affinity increased going from a more negative to a more positively charged metal binding environment suggested the involvement of hydrogen bonding and salt-bridging interactions. We proposed a rack-induced binding environment, similar to that suggested for blue copper electron-transfer proteins.[51] In this model, the protein matrix constrains the metal coordination environment, thereby leading to changes in the stability of the different oxidation states, which are exploited to tune the redox potential of the copper center. Our results suggest that, in our model CuNiR, this induced-rack effect is greater for the Cu^{I} oxidation state. We proposed a hydrogen-bonding interaction between Glu22 and His23 that orients the imidazole ligand is responsible.

Finally, we examined the series of models with outer-sphere modifications for CuNiR rates, using the ascorbate assay described above. As the charge was decreased from 0 to −12, we observed a fourfold increase across the series in NiR activity and a correlation with the reduction potential (Figure 8B). At pH 5.8, the higher the reduction potential of our outer-sphere models, the lower the rate. Although this appears to show a linear trend linking the rate to the reduction potential, the assay conditions, in which ascorbate is added in significant excess, invalidate the conclusion that this is due to electron-transfer rates, as we have shown that the reduction of Cu^{II} to Cu^{I} by ascorbate is not rate-limiting. Instead, we suggest that the reorganization energy upon oxidation (from trigonal Cu^{I} to pseudo-tetrahedral Cu^{II}) limits the observed rate. This study established that changes in the charge environment around the active site, through residue substitutions at positions nearby, can be used to modify properties that influence reduction potentials and NiR activities in a systematic fashion.

3.4. Modification of the Steric Bulk and Addition of Potential Hydrogen-Bonding Residues in the Inner Sphere

Having established the influence of outer-sphere modifications on CuNiR activity, we then turned to examining the role of inner-sphere modifications. It is well-known that inner-sphere residues of an enzyme play significant roles in catalysis, and mutations of inner-sphere residues have been shown to significantly alter catalytic rates and efficiencies. Therefore, using our rational design strategy, we identified two positions in the 3SCC where substitution of the Leu layer by other residues (Figure 6B) could lead to modification of the coordination environment of the bound Cu or Cu-coordinated water molecule(s). We had previously shown that we could control the coordination number of Cd bound to tris(cysteine) sites by modifying the steric bulk of the hydrophobic layer spacing in the core above or below the $Cd(S_3)$ binding site.[16,52] Thus, by modification of the steric bulk around a catalytically active metal binding site, we should be able to tune the substrate and solvent access.

By using this approach with our $Cu(His_3)$ NiR site, we substituted leucine residues in positions 19 and 26, the leucine layers directly above and below the Cu(NiR) site (Table 4 and Figure 6B).[53] We increased the steric bulk above the Cu binding site by substitution with isoleucine or D-leucine, as our first-generation CuNiR model was thought to be five-

coordinate in the cupric state (compared to four-coordinate for native CuNiR), and we believed that increasing the bulk above the metal binding site would decrease solvent access and lower the coordination number of the Cu center. We then tested the effect of decreased steric bulk above or below by substitution with alanine, as crystal structures of our heavy-metal binding scaffolds have shown that decreased steric bulk can permit up to four additional water molecules.[34] Finally, to study the effect of hydrogen bonding to the Cu-coordinated water molecule(s) or histidine imidazole ligands and/or the addition of extra Cu-coordinating residues, we made scaffolds that positioned aspartate above or below the copper site.

We examined this series of CuNiR models for CuNiR activity and observed rate constants that split the series into two identifiable groups (Figure 9, green bars)—those whose CuNiR initial rate constants were approximately the same as the parent TRI-H (L19I and $L19_DL$), and those whose CuNiR rate was between 60- to 75-fold greater (Ala and Asp substitutions). We believed that this trend in rate differences between the two groups was due to structural differences in the resting state of the Cu^I forms, as we have shown that the reduction of the Cu^{II} species is extremely rapid under our assay conditions. Therefore, we collected X-ray absorption data and compared the 1s→4p energies in the XANES region (Figure 10) as well as bond lengths from EXAFS data.

The increase in the intensity of the Cu^I pre-edge, as well as increases in the copper–ligand bond lengths from EXAFS data upon decreasing the steric bulk around the binding site, suggests that rather than permitting extra coordinating ligands to bind to the copper site, the reduction in the steric bulk allows the Cu^I state to relax and reduce the coordination number from 3 to 2. This was the opposite of what we had observed when we modified the steric bulk surrounding heavy-metal binding sites, where decreased steric bulk led to an increase in the coordination number. We observed that the

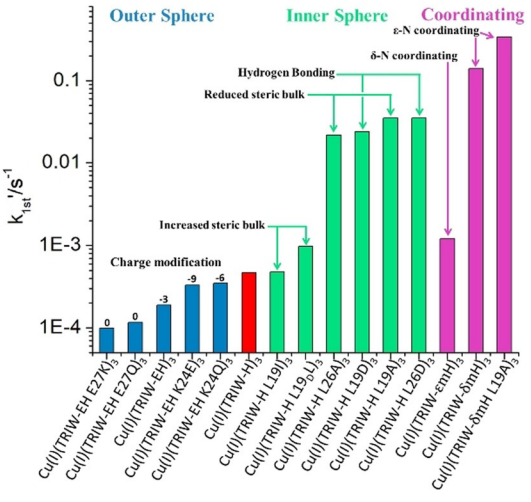

Figure 9. Pseudo-first-order rate constants of the original TRIW-H construct (red) reported in Ref. [37] compared to the outer-sphere helical interface residues (blue) reported in Ref. [50], interior residues (green) reported in Ref. [53], and primary coordinating residues (magenta) reported in Ref. [56]. Reprinted and adapted from Ref. [56] with permission. Copyright 2019 American Chemical Society.

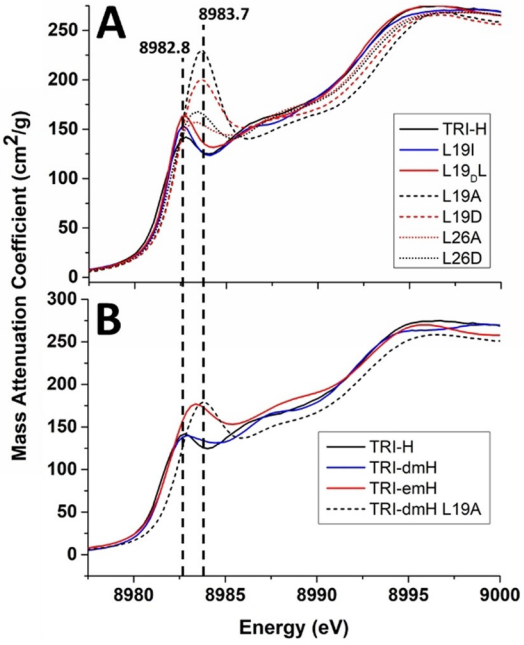

Figure 10. Cu^I XANES at pH 5.8 of A) inner-sphere modifications and B) primary coordinating modifications compared to that of TRIW-H. Adapted and reprinted from Refs. [53] and [56] with permission. Copyright 2018 Wiley-VCH and 2019 American Chemical Society.

XANES 1s→4p energies could accurately define the two groups, with the more active constructs showing a shift to higher energy compared to the parent TRI-H, and those whose rates were approximately the same and also had similar 1s→4p energies. This energy shift, which provides information on the electron density around the copper site and thus its ability to participate in redox chemistry, appears to correlate with the increase in the NiR activity, and would also have an impact on the potential energy landscape of the transition state during catalysis (see Section 3.2). Native CuNiRs have a four-coordinate $Cu(His)_3(H_2O)$ in both the oxidized and reduced states, thus suggesting that the reorganization of our model copper binding sites may be a limiting factor in our activity enhancements.

3.5. Role of Histidine Coordination Isomers in CuNiR Activity

Another significant feature of imidazole moieties is the potential for either of the imidazole nitrogen atoms to be the coordinating ligand. As already mentioned in our discussion on PHM and CuNiR, these two enzymes display vastly different copper chemistry, but possess the same Cu(His)3 copper environment. Close inspection of the structures of CuNiR (PDB: 4YSE[54]) and PHM (PDB: 1PHM[55]) reveals different tautomeric coordinative isomers, with the former coordinating copper through the N_ε atom and the later through the N_δ atom of the imidazole. The difference in coordination (N_ε versus N_δ) has been shown to be common in type 1 Cu sites showing electron-transfer versus catalytic type 2 Cu sites. To determine the orientation of the histidine

coordination in our CuNiR model (TRI-H), we designed scaffolds that included N-methylated histidine as the primary coordinating ligands (sequences in Table 4).[56] Thus, we could compare N_ε-methylhistidine (TRI-$_{\varepsilon m}$H, coordinating through N_δ) with N_δ-methylhistidine (TRI-$_{\delta m}$H, coordinating through Nε) to our original design and elucidate not only the coordination state, but also the effect of forcing the flipped coordination mode, thereby determining directly the influence of copper–histidine coordination isomers on properties of our well-understood metalloezymatic system.

It is important to note here that methylation of the imidazole fundamentally alters the properties of the ligand, not limited to only the N-coordination. The replacement of one of the N–H moieties by N–Me removes an opportunity for hydrogen bonding and changes the pK_a value and accessible charge of the ligand. Furthermore, the methyl group is a much stronger electron donor, changing the electronic nature of the imidazole ligand, often in ways that are difficult to predict.[57] Finally, *N*-methylimidazoles are much more sterically demanding than the parent histidine groups, which could have a significant impact on the geometry and stability of our Cu sites. Thus, there are numerous factors that have to be taken into account when considering substitution with *N*-methylhistidine.

We characterized the effect on forced ε- or δ-nitrogen coordination (by methylation of the other imidazole nitrogen atom) on the geometry, redox potential, and catalytic activity of the copper binding site. EPR, XAS, and UV/Vis spectroscopic data suggested that TRI-$_{\varepsilon m}$H has a lower number of coordinating imidazole ligands than TRI-$_{\delta m}$H for both the Cu^I and Cu^{II} states (Figure 11). Significantly, TRI-$_{\delta m}$H more closely mimicked the geometric features of the original TRI-H, with TRI-$_{\varepsilon m}$H showing more of a tetrahedral nature for the Cu^{II} species (N_3O versus N_2O_2 coordination environment for TRI-H and TRI-$_{\delta m}$H) and more two-coordinate character for the Cu^I species in contrast to the three-coordinate character of the other two. These data suggest that the parent TRI-H coordinates with the ε-nitrogen atom. As with our inner-sphere modifications, we observed a shift in the 1s→4p energy in the XANES region, with TRI-$_{\delta m}$H matching the energy of the parent, whereas TRI-$_{\varepsilon m}$H is slightly higher in energy (Figure 10B).

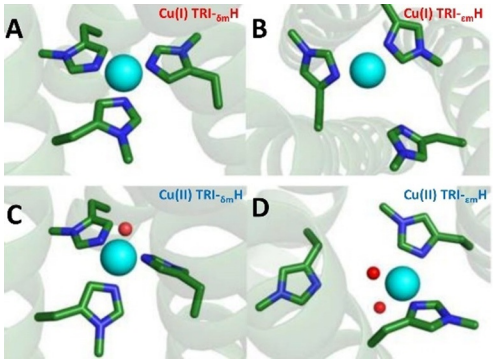

Figure 11. Models of the metal binding sites of A) Cu^I-TRIW-δmH and B) Cu^I-TRIW-εmH, C) Cu^{II}-TRIW-δmH, and D) Cu^{II}-TRIW-εmH. Models were made using the program PyMol and based on the $Zn^{II}(His)_3$ site of $Hg^{II}{}_SZn^{II}{}_N$ $(CSL9CL23H)_3$ [PDB: 3PBJ[12]]. Reprinted and adapted from Ref. [56] with permission. Copyright 2019 American Chemical Society.

Finally, we compared the NiR activity of the *N*-methylhistidine-containing scaffolds to our previous designs (Figure 9, magenta). We observed the largest increase in NiR activity through modification of the primary coordinating ligands. Interestingly, the largest enhancement in rate came from methylation of the δ-nitrogen atom, which forced ε-nitrogen coordination, the same as in TRI-H. We concluded that an inductive-like effect upon N-alkylation, linked to increases in the HOMO energy from more electron-rich ligands, accounted for the difference between the two scaffolds. We attempted to combine the features that generated the best NiR activities from the previous inner-sphere modifications (reduction of steric bulk through L19A mutation, 75-fold increase in rate compared to TRI-H) with the best primary coordinating substitution (TRI-$_{\delta m}$H, 260-fold rate enhancement) to give TRI-$_{\delta m}$H L19A. Although this only resulted in a modest 2.5-fold increase in rate versus that of the TRI-$_{\delta m}$H, this scaffold is the best CuNiR model to date in a homogeneous aqueous system, with a 640-fold rate enhancement compared to our first generation CuNiR, TRI-H. Although this is currently the best synthetic homogeneous copper catalyst for CuNiR activity, the rate is 400000-fold lower than the native system.

Michaelis–Menten kinetics analysis of the CuNiR activities of our models revealed that this decreased activity is due to factors that impact both the maximal catalytic rate as well as substrate access and binding (Table 5). The V_{max} value plateaus, while the biggest influence on catalytic efficiency arises from K_M effects. Again, we have thus far not included the critical acid-base catalyst, an aspartate that is important in the activity of the native protein, in our CuNiR models. We have already attempted to add a nearby Asp residue, but the enforced threefold symmetry meant that three Asp residues were positioned near the $CuHis_3$ site, and we believe that those aspartate residues interacted with each other rather than with the Cu site.[53] Additionally, we observed a significantly decreased K_M value compared to small-molecule models, which suggests that substrate recognition and access is limited in our scaffold design. This difference may also reflect NO_2^- binding to Cu^I over Cu^{II} and suggests we need to make future alterations that enhance substrate binding, such as new scaffolds that will allow for asymmetric modification of the scaffold. We have developed such a scaffold, which will be described soon.[63]

4. Design of Electron-Transfer Sites in De Novo Scaffolds

We now turn to the discussion of our recent developments in the de novo design of electron-transfer sites in our alpha-helical scaffold systems. Metal binding sites that transfer electrons across membranes, between metal binding sites, or coupled to proton transfers require metal binding sites that can support the different geometric and ligand preferences of the different redox states, as is the case for metal binding sites

Table 5: Kinetic parameters for CuNiR activity for select 3SCCs and small-molecule model complexes at pH 5.8.

Construct	Rate[a] [s^{-1}]	V_{max} [$M\,s^{-1}$]	K_M [M]	k_{cat} [s^{-1}]	k_{cat}/K_M [$s^{-1}\,M^{-1}$]
TRIW-H[58]	4.6×10^{-4}	N/A	N/A	N/A	N/A
TRIW-H L19A[59]	3.5×10^{-2}	$2.3\pm0.3\times10^{-6}$	0.24 ± 0.05	0.23 ± 0.03	1.0 ± 0.3
TRIW-$_{\delta m}$H	0.12	$1.5\pm0.1\times10^{-5}$	0.18 ± 0.02	1.5 ± 0.1	8.2 ± 0.1
TRIW-$_{\delta m}$H L19A	0.30	$1.5\pm0.1\times10^{-5}$	0.13 ± 0.01	1.5 ± 0.1	11.3 ± 0.1
TRIW-$_{\varepsilon m}$H	1.2×10^{-3}	N/A	N/A	N/A	N/A
$[CuMe_2bpa(H_2O)(ClO_4)]^+$ on electrode pH 5.5[60]	N/A	N/A	1.1×10^{-3}	0.063	57.3
$[CuMe_2bpa(H_2O)(ClO_4)]^+$ in solution pH 5.5[60]	N/A	N/A	2.5×10^{-3}	5.3×10^{-5}	0.02
*Af*CuNiR pH 6.5[61]	N/A	N/A	1.5×10^{-4}	620	4.1×10^{6}
*Ax*CuNiR pH 7.0, 4 °C[62]	N/A	N/A	2.7×10^{-3}	89	3.3×10^{5}

[a] The value of the rate constant refers to the pseudo-first-order rate constant for the metallopeptide-catalyzed reduction of nitrite by ascorbate in solutions containing 30 mM nitrite and 1.2 mM ascorbate. N/A = not determined/not available.[58]

involved in redox cycling in a catalytic site, such as CuNiR. As discussed in more detail above, this requires careful consideration of the coordination number and geometry as well as ligand positioning within the scaffold. We will highlight the development of our models for iron-containing rubredoxins and copper-containing cupredoxins.

4.1. Development of Non-Heme Iron Rubredoxin Models

FeS cluster proteins are a class of proteins with cofactors of varying complexity ranging from a single Fe atom bound by four cysteine residues (ex. rubredoxin)[64] to multiatom cofactors that must be assembled by separate protein machinery before being inserted into the final target protein (ex. the P cluster of nitrogenase).[65] The relative simplicity of rubredoxin and the extensive literature available on its geometry and spectroscopic properties make an attractive target for metalloprotein design.[3b]

Previous attempts to design rubredoxin focused on replicating the hairpin of the native binding site to show that the same secondary structure and metal binding site could be created using a de novo protein sequence.[66] The Regan group used the program Metal Search to put a tetrahedral Cys_4 site into the B1 domain of IgG-binding protein G, but although this construct was able to recapitulate the Fe^{III} spectroscopic properties of rubredoxin it was not a functional redox center.[66d] The DeGrado group. created a rubredoxin mimic by recapitulating the local secondary geometry around the Fe in the native protein and minimizing the surrounding protein needed to maintain this geometry to a 40 amino acid peptide.[66b] This construct not only successfully mimicked the Fe^{III} spectroscopic properties of native rubredoxin, but was the first de novo rubredoxin mimic capable of reliable redox cycling up to 16 cycles. Arguably the most successful simplification of rubredoxin was created by the Sénèque group within a 18 amino acid peptide composed of a cyclic portion and a linear tail.[66a] Although this construct was capable of less redox cycles than the model developed by the DeGrado group (7 compared to 16), it successfully recreated the Fe^{II} and Fe^{III} spectroscopic properties of native rubredoxin with less than half of the amino acids.

We focused our efforts on determining whether this hairpin turn secondary structure was necessary to recapitulate the spectroscopic properties of a rubredoxin by implanting a rubredoxin-type Cys_4 binding site within an alpha-helical bundle (Figure 12).[67] Our group had previously designed two Cys_4 proteins based on the heavy-metal binding Cys_3 peptide α_3DIV (α_3DIV H72C or L21C) as models for the Cd binding site of CadC.[68] By using ^{113}Cd NMR spectroscopy we determined that the H72C variant, which positioned the fourth Cys in a nearby loop region, formed CdS_3O while L21C, which positioned the fourth Cys as part of a CXXC chelate motif, formed CdS_4. We tested both α_3DIV H72C and L21C as prospective rubredoxin models.

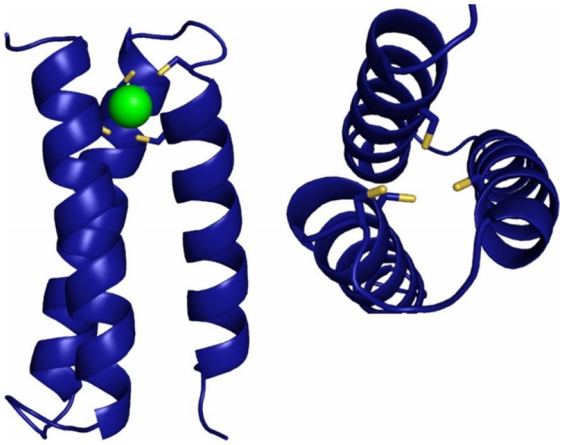

Figure 12. Model of the synthetic rubredoxin, Fe-α3DIV L21C, constructed in PyMol based on the NMR structure of α3DIV (PDB: 2MTQ). Reproduced from Ref. [67] with permission. Copyright 2018 American Chemical Society.

When expressing α_3DIV H72C and L21C in media containing supplemental Fe, the lysate of the L21C variant was red in color, thus indicating some level of Fe incorporation in vivo. Similar expressions of either α_3DIV alone or its H72C variant gave a standard yellowish color. Hence, our characterization efforts focused on α_3DIV L21C as a possible rubredoxin mimic using UV/Vis, Mössbauer, EPR, magnetic circular dichroism (MCD), and X-ray absorption spectroscopy. Purified peptide was reconstituted with Fe by the addition of Fe^{II} before oxidizing in air to produce the Fe^{III} form. The optical absorption spectra of Fe^{III}-α_3DIV L21C showed

Table 6: Physical properties of constructs reported in Ref. [67].

Protein	UV/Vis: λ [nm] (ε [$M^{-1}cm^{-1}$]	Redox potential (vs. NHE) [mV]	Fe^{III} Mössbauer (δ and ΔEQ [$mm\,s^{-1}$], D [cm^{-1}], A [T])	Fe^{II} Mössbauer (δ and ΔEQ [$mm\,s^{-1}$], D [cm^{-1}], A [T])
rubredoxin[69,70]	750 (350) 570 (3200) 490 (6600) 370 (7710)	−90 to +50	$\delta/\Delta EQ = 0.24/-0.5$, $\eta = 0.2$ $D = +1.9$, $E/D = 0.23$ $A_{xx,yy,zz} = (-16, -15.9, -16.9)$	$\delta/\Delta EQ = 0.70/-3.25$, $\eta = 0.65$ $D = +7.4$, $E/D = 0.28$ $A_{xx,yy,zz} = (-20.1, -8.3, -30.1)$
α_3DIV L21C	595 (1200) 491 (2700) 345 (5000)	−75 (pH 8.5)	$\delta/\Delta EQ = 0.26/-0.5$, $\eta = 0.0$ D = +0.5, E/D = 0.15 $A_{xx,yy,zz} = (-15.9, -16, -17)$	$\delta/\Delta EQ = 0.73/-3.40$, $\eta = 0.9$ $D = +7$, $E/D = 0.26$ $A_{xx,yy,zz} = (-16, -7.3, -25)$

ligand-metal charge-transfer (LMCT) bands at similar energies as native rubredoxin (Table 6), but with about 30% of the expected intensity, consistent with other spectroscopic data, which would indicate some proportion of contaminant within the construct (see below).[69]

MCD analysis enabled the optical spectrum of Fe^{III}-α_3DIV L21C to be deconvoluted to nine unique peaks that matched in energy to those seen in native rubredoxin. Further investigation of the optical spectrum through MCD at variable temperatures and variable fields determined the saturation behavior to be consistent with that of native rubredoxin. Mössbauer spectra of Fe^{II}-α_3DIV L21C recorded at 4.2 K were consistent with those of native rubredoxin, but high-field spectra revealed two unique components: 60% FeS_4 and 40% FeS_3O.[70a] The Mössbauer results of Fe^{III}-α_3DIV L21C were similar, with the bulk of the sample showing similar spectra as rubredoxin but 25% of the sample was concluded to be impurities of ferric oxides/hydroxides. This impurity was also observed in the X-band EPR spectrum, although it was largely consistent with native rubredoxin. Lastly, EXAFS analysis revealed that Fe^{II}-α_3DIV L21C was dominated by a single distance Fe–S scatterer bond distance of 2.32 Å.

We analyzed the electrochemistry of Fe^{II}/Fe^{III}-α_3DIV L21C to investigate its activity as an electron-transfer site and determined a one-electron transfer with a potential of −75 mV, which falls within the −90 to 50 mV range seen in native rubredoxins.[64a,f,70b,71] pH-dependent studies of the redox potential found it was a coupled 2-proton-1-electron event. This differs from native rubredoxins whose redox potentials are independent of the pH value. We hypothesize that charged residues near the metal binding site of our construct may be the cause of this effect. Chemical reduction with dithionite followed by oxidation in air could be cycled up to three times before the construct was irreversibly bleached, likely caused by the oxidation of cysteine.

This characterization effort was the most robust ever undertaken for a designed rubredoxin and showed that one can construct a tetrahedral FeS_4 center within a rigid scaffold unrelated to the native secondary structure. We also determined that the CXXC motif of native rubredoxins is an important part of maintaining this metal binding geometry within a protein, as our scaffold without this motif was unable to recapitulate the spectroscopic properties of a tetrahedral FeS_4. Comparison of the MCD data with the results from the Mössbauer and EPR studies showed that our construct also reaffirms the *D*-sign controversy seen in native rubredoxins, in which MCD favors a negative value while Mössbauer and EPR favor a positive value.[70a,72] Moving forward, high-field EPR spectroscopy and further protein design of this construct should be used to investigate this apparent disagreement.

4.2. Development of Cupredoxin Models

Type 1 Cu proteins are electron-transfer proteins with a Greek key beta barrel fold and a $CuHis_2CysXxx$ binding site, in which Xxx can vary between Met, Gln, and (in one instance) Glu. These proteins have long fascinated the bioinorganic community because of their constrained geometry, unique optical properties that lead to bright blue, green, or red solutions, and compressed hyperfine coupling constants in their EPR spectra.[73] Blue type 1 Cu proteins have an intensive LMCT band at 600 nm which is assigned as a Cys-Cu π-$d_{x^2-y^2}$ transition, a short Cu–Cys bond of 2.1–2.2 Å, and compressed hyperfine coupling constants $A_\parallel$ below $100 \times 10^{-4}\,cm^{-1}$.[74] Green type 1 Cu proteins have an additional LMCT band at 450 nm, which is assigned as a Cys-Cu σ-$d_{x^2-y^2}$ transition, with a ratio between the two intensities of around one, a slightly longer Cu–Cys bond of 2.2 Å, and similarly compressed hyperfine coupling constants $A_\parallel$.[75] Finally, red type 1 Cu proteins have a much more intense σ-LMCT band at 390 nm, a blue-shifted and diminished Cys-Cu π-$d_{x^2-y^2}$ transition at 500 nm with a ε_σ/π ratio of about 3, an EPR spectrum similar to that of type 2 Cu proteins, and Cu–Cys bonds closer to 2.3 Å.[76]

Previous efforts to design type 1 Cu proteins in scaffolds unrelated to the native structures have largely produced green copper proteins.[77] The Valentine group showed that they could recreate the spectroscopic properties of a green copper protein with a H80C variant of Cu/Zn superoxide dismutase, while Hellinga created a series of thioredoxin variants capable of recreating the spectroscopic properties of green copper proteins upon the addition of the exogenous ligand azide.[77a,b] By using a combinatorial approach, the Hildebrandt group created and screened 180 different His_2Cys motifs containing four helical bundle peptides and found several that had the characteristic spectroscopic properties of green copper proteins.[77c] The most successful studies towards a de novo blue copper protein were those of the Tanaka group, who modified a previous His_2Glu Cu binding protein within a four helical bundle scaffold to make a His_2Cys binding site and successfully generated a green copper protein by rational design.[77d] Interestingly, the

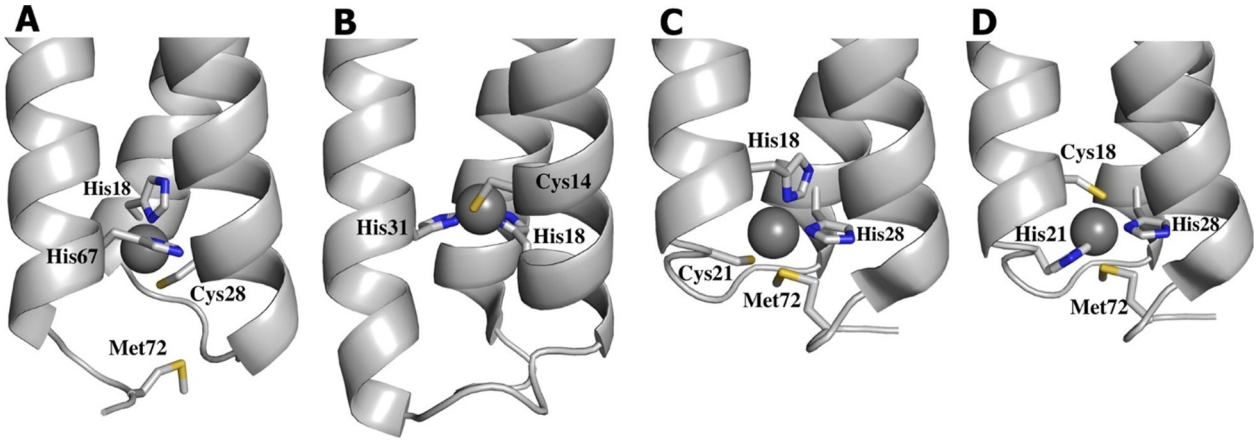

Figure 13. Models of the reduced state based on the EXAFS analysis of the designed cupredoxins. A) $Cu^{I}\alpha_3$DCR1, B) $Cu^{I}\alpha_3$DChC2, C) $Cu^{I}\alpha_3$DCH3, D) $Cu^{I}\alpha_3$DCH4. Reproduced from Ref. [79] with permission. Copyright 2015 American Chemical Society.

addition of several exogenous ligands such as chloride, sulfate, acetate, and phosphate were shown to tune this green copper into a blue copper spectroscopically.[78] Although all these studies were impressive and pushed the field forward, the need for an exogenous ligand to recapitulate the spectroscopic properties of a blue copper protein meant that the question of how one could design a self-contained blue copper protein in a de novo scaffold remained unanswered.

We had previously shown that a His_3 or Cys_3 metal binding site could be designed into the 3HB protein α_3D, but this was our first attempt at a mixed coordination sphere.[24,80] Four different prospective cupredoxins were designed into the α_3D scaffold: CR1, CH3, CH4, and ChC2 (Figure 13 and Table 7).[79] α_3DCR1 incorporates a His2Cys binding site that spans the three helices at residues 18, 28, and 67 (the same positions previously used for α_3DIV and α_3DH3) with a nearby Met residue at position 72. α_3DCH3 and α_3DCH4 were designed with chelate motifs of CXXH or HXXC, respectively, on helix 1, with the His and Met ligands divided between the two remaining helices. Lastly, the α_3DChC2 design repositions the metal binding site of α_3DCH4 further towards the N-terminus of the peptide and the center of the hydrophobic core and encloses it within a "box" of hydrophobic residues in an attempt to enforce an entatic or rack state similar to native type 1 Cu proteins.

Denaturation with GuHCl followed using circular dichroism spectroscopy showed that, with the exception of α_3DChC2, all four constructs were alpha-helical and stably folded in solution. UV/Vis and EPR spectroscopic studies on the Cu^{II} form were carried out to determine how well each construct had recapitulated the Cu^{II} geometry of a type 1 Cu protein. α_3DCR1 exhibited spectra similar to those of a type 2 copper-thiolate species with a pronounced LMCT band at 380 nm and a shoulder at 550 nm with a $\varepsilon_{\sigma/\pi}$ ratio of 3.6 and a hyperfine coupling constant of $163\times10^{-4}\,cm^{-1}$. α_3DCH3 formed a yellow species with an intense band at 400 nm and a broad band between 600 and 800 nm, which resulted in an extremely high $\varepsilon_{\sigma/\pi}$ of 11.9 and a hyperfine coupling constant of $152\times10^{-4}\,cm^{-1}$. α_3DCH4 had absorption bands at 377, 450, and 520 nm with a $\varepsilon_{\sigma/\pi}$ ratio of 3.3 and a hyperfine coupling constant $A_{\parallel}$ of $185\times10^{-4}\,cm^{-1}$. Interestingly, a simple flip of a chelate motif from CH3 to CH4 had drastically changed the spectroscopic properties of the Cu^{II} species. We hypothesized that this change was caused by the more buried position of the Cys metal binding site when this chelate motif was flipped. This led to the design of α_3DChC2, in which this Cys residue is buried even further, and attempted to create a hydrophobic box around the bound Cu center. α_3DChC2 has two intense bands at 401 and 499 nm with $\varepsilon_{\sigma/\pi}=2.2$ and a slightly compressed hyperfine coupling constant of $130\times10^{-4}\,cm^{1}$ resulting in a red-brown copper species. The optical properties of this construct is reminiscent of blue

Table 7: Physical properties of constructs reported in Ref. [79].

Protein	UV/Vis: λ [nm] (ε [$M^{-1}cm^{-1}$])	EPR: $A_{\parallel}\times10^{-4}\,cm^{-1}$	Redox potential (vs. NHE) [mV]
α_3DCR1	380 (1565), 550 (438), 600—800 (300) $\varepsilon_{\sigma/\pi}=3.6$	163	+398
α_3DCH3	400 (2619), 600–800 (300) $\varepsilon_{\sigma/\pi}=11.9$	152	+364
α_3DCH4	377 (1840), 450 (1098), 520 (600), 600–700 (380) $\varepsilon_{\sigma/\pi}=3.3$	185	+399
α_3DChC2	401 (4429), 499 (2020), 600–700 (550) $\varepsilon_{\sigma/\pi}=2.2$	130	+462
plastocyanin[81]	460 (400), 597 (5200) $\varepsilon_{\sigma/\pi}=0.05$	63	+372
Ac nitrite reductase[40,75]	457 (2590), 570 (1490) $\varepsilon_{\sigma/\pi}=1.7$	73	+247
nitrosocyanin[76,82]	390 (7000), 570 (2200) $\varepsilon_{\sigma/\pi}=3.2$	144	+85

copper protein variants such as M121E azurin or M148E rusticyanin as well as the native red copper protein nitrosocyanin.[82–83]

One of the most striking results from this study was that all four constructs recapitulated the Cu^{I} geometry of a blue copper protein regardless of how successful that construct was at recapitulating the Cu^{II} geometry and spectroscopic properties. EXAFS data for the Cu^{I} species of all four constructs showed short Cu–Cys bond lengths between 2.18 and 2.22 Å with long-distance scatterers observed from His ligation. Analysis of the Cu^{I} XANES 1s→4p transition at 8984 eV of all four constructs divided the constructs into two groups: the copper centers in ChC2 and CR1 being more 3-coordinate, while those in CH3 and CH4 were more 4-coordinate. With potentials ranging between 364 and 462 mV, protein film voltammetry determined that all four constructs were also successful in modeling the redox potential of a blue copper protein, which typically range from 300 to 730 mV.[81b,83b,84]

These studies showed that the design of the cupredoxin site within a 3HB could have drastic effects on the spectroscopic properties of the bound Cu^{II} ion. Our designs culminated in α_3DChC2, which successfully recapitulated the spectroscopic properties of a red copper protein with a Cu^{I} geometry and the redox potential of a blue copper protein. We postulated that a more complete understanding of the metal binding site created by α_3DChC2 would allow us to tune the spectroscopic properties of this Cu^{II} construct to those of a green or blue copper protein. That the Cu^{I} geometry and redox potential of these constructs remained invariant across our designs indicates that if one were able to tune the spectroscopic properties of the Cu^{II} form of the construct towards those of a blue copper protein, the other parameters would already be in place.

Our success with recapitulating a red copper protein with α_3DChC2 lead us to revisit this construct to gain clues to how it might be tuned into models for green or blue copper proteins. One possibility was that the relative instability of α_3DChC2, as determined by chemical denaturation, may have weakened the hydrophobic box meant to create an entatic state. This instability also precluded any single site mutation studies to investigate this construct, so a more stable variant was necessary. Our experience with three-stranded coiled coils led to the strategy of increasing the length of the α_3D alpha helix in the scaffold protein to improve the thermodynamic stability.[85] The initial design of the α_3D scaffold by the De Grado group went through several iterations of redesign, largely centered around the loop region connecting each helix. For our design of GRα_3D we sought to avoid this complication by expanding the helices from the center and duplicating the central heptad of each. GuHCl denaturation of GRα_3D proved this strategy was successful, creating a scaffold with a free energy of unfolding of 11.4 kcal mol^{-1} compared to the 5.9 kcal mol^{-1} of the parent α_3D. This increased stability allowed us to grow diffraction-quality crystals and solve the structure of the scaffold to a resolution of 1.34 Å (Table 8).

By designing the ChC2 binding center into GRα_3D we created GRα_3DChC2 and determined it to be fully folded in solution, unlike its parent peptide (Figure 14). The spectroscopic properties of the Cu^{II} form of this construct, however, remained decidedly within the category of a red copper protein, thus negating the hypothesis that thermodynamic instability had been the cause of the aberrant spectral properties of α_3DChC2. MCD deconvolution of the optical spectrum of GRα_3DChC2 further cemented this red copper protein assignment, matching the d-d electronic transitions observed in native nitrosocyanin.[76] The $His_2CysGlu$ binding site of nitrosocyanin was not a part of our original α_3DChC2 design so the question remained as to why this construct was so similar to nitrosocyanin when it was designed solely as a His_2Cys binding site.

Modeling the copper binding site of GRα_3DChC2 into the GRα_3D X-ray crystal structure suggested that, because the binding site was designed to span two of the three helices, the Cu atom would be positioned off-center from the hydrophobic interior and would likely locate more towards the helical-helical interface. This positioning of the Cu center would bring it within 5 Å of Glu41, included in the GRα_3D scaffold as part of a salt bridge with Arg24. This was

Table 8: Physical properties of constructs reported in Ref. [11].

Protein	UV/Vis: λ [nm] (ε [M^{-1} cm^{-1}])	EPR: $A_{\parallel}\times10^{-4}$ cm^{-1}	Redox potential (vs. NHE) [mV]
GRα_3DChC2	400 (3760), 490 (1600) $\varepsilon_{\sigma/\pi}=2.3$	142	+530
GRa3DChC2 R24A	399 (2520), 490 (1150) $\varepsilon_{\sigma/\pi}=2.2$	142	–
GRa3DChC2 R24M	399 (3480), 493 (1450) $\varepsilon_{\sigma/\pi}=2.4$	138	–
GRa3DChC2 E41Q	377 (5120), 490 (970) $\varepsilon_{\sigma/\pi}=5.3$	154	+510
GRa3DChC2 E41A	373 (4090), 490 (720) $\varepsilon_{\sigma/\pi}=5.7$	160	+510
nitrosocyanin[76,82]	390 (7000), 490 (2200) $\varepsilon_{\sigma/\pi}=3.2$	142	+85

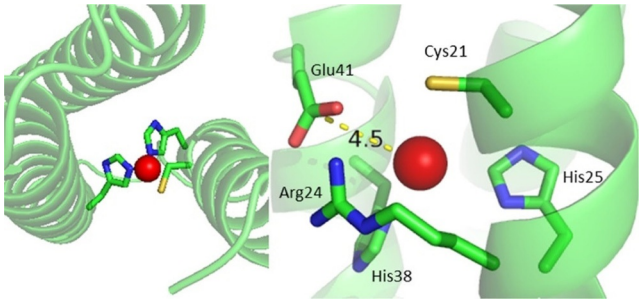

Figure 14. PyMol illustrations showing the expected position of the metal binding site of GRα3DChC2 (left) and the expected Glu41-Cu distance if Cu^{II} were bound in such a position. Reproduced from Ref. [11] with permission. Copyright 2018 American Chemical Society.

a particularly intriguing possibility as the absorption spectrum of GRα_3DChC2 resembled that of not only nitrosocyanin but the variant blue copper proteins M121E azurin and M148E rusticyanin. Thus, we hypothesized that removing this Cu-Glu41 interaction through a E41A mutation or tuning it with E41Q would allow us to tune the spectroscopic properties of GRα_3DChC2 to that of a blue or green copper protein.[82,83]

Mutation studies around this Glu41-Arg24 pair found that E41A and E41Q caused drastic changes to the absorption profile: blue-shifting the σ-LMCT band and increasing the $\varepsilon_{\sigma/\pi}$ value to 5.3 or 5.7, respectively, while the hyperfine coupling constant increased to 160 or 154×10^{-4} cm^{-1}, respectively. These changes indicated a change from a red copper protein to a type 2 Cu protein. R24A and R24M constructs were made to test if the effects of the E41 mutations were caused by the loss of a salt bridge and increased solvent access rather than the loss of a direct interaction between Cu and E41. R24 variant constructs showed no change in the UV/Vis and EPR spectra of their Cu^{II} forms, thus confirming that the E41A and E41Q mutations had specifcally disrupted an E41-Cu interaction. This result confirmed that our GRα_3DChC2 construct was best thought of as a nitrosocyanin mimic rather than a blue copper protein with a Glu ligand in the axial position. This means that tuning this construct to have the spectroscopic properties of a blue copper protein will likely require larger changes to the active site. This could possibly be achieved by mirroring a recent construct made by the Lu group in which the blue copper protein Azurin was mutated to a nitrosocyanin-like red copper construct through rotation of the active site and substitution of the fourth Cu ligand.[86] The Cu^{I} geometries and redox potentials were found to be invariant in all of the mutations tested within our study. This reaffirms the prior assumption that one can focus on tuning the Cu^{II} spectroscopic properties with a reasonable expectation that this will not impact the Cu^{I} geometry or redox potential. We have since used this new structural insight to create variants with spectroscopic properties corresponding to a green copper protein that could be tuned to a blue copper protein using chloride as an exogenous ligand—similar to the work of the Tanaka group as well as a variant that recapitulates the spectroscopic properties of blue copper proteins without the need for an exogenous ligand.[77d] A manuscript describing this work is in preparation.[87]

4.3. Measuring Electron-Transfer Activity

One of the overarching goals of our group has been to create a fully functional and self-contained Cu nitrite reductase with an active type 2 Cu site and an electron-transfer site. This goal requires an understanding of how electron transfer occurs through our peptides as well as the rates of electron transfer at their redox-active metal centers. To date we have explored this in two ways: using intermolecular electron transfer to study α_3DCH3 and intramolecular electron transfer to look at how electrons can travel through our constructs.[88]

To investigate the electron-transfer properties of one of our cupredoxin models, solutions of α_3DCH3 were photooxidized by irradiating ruthenium(II) trisbipyridine, $[Ru^{II}(bipy)_3]^{3+}$, with 460 nm laser light in the presence of the electron acceptor $[Ru^{III}(NH_3)_6]^{3+}$ to produce $[Ru^{III}(bipy)_3]^{3+}$, a powerful oxidizing agent with a reduction potential of 1.3 V. Electron transfer between different species was then followed by optical spectroscopy (Figure 15 and Table 9). In this reaction, the $[Ru^{II}(bipy)_3]^{3+}$ radical is formed after 100 ns and this reacts with the electron acceptor to form $[Ru^{III}(bipy)_3]^{3+}$ after 1 μs. A positive absorption band at 400 nm after 100 μs was assigned as the formation of $Cu^{II}\alpha_3$DCH3 from the spectroscopically silent $Cu^{I}\alpha_3$DCH3. This $Cu^{II}\alpha_3$DCH3 reacted with the electron acceptor to reform $Cu^{I}\alpha_3$DCH3 after 10 ms. Based on the changes in the absorption, we estimated that around 1.9 μM $Cu^{II}\alpha_3$DCH3 was formed from 3 μM $[Ru^{III}(bipy)_3]^{3+}$. Reactions using other photoactive oxidants followed similar profiles.

Kinetic analysis found that the first order rate constant of the intermolecular electron-transfer reaction between $Ru^{III}(bipy)_3$ and $Cu^{I}\alpha_3$DCH was 1.15×10^5 s^{-1}, four times greater than the same reaction with apo-peptide. This first order rate constant varied between 0.79 and 1.15×10^5 s^{-1} depending on the photooxidant used. We hypothesized that the reaction

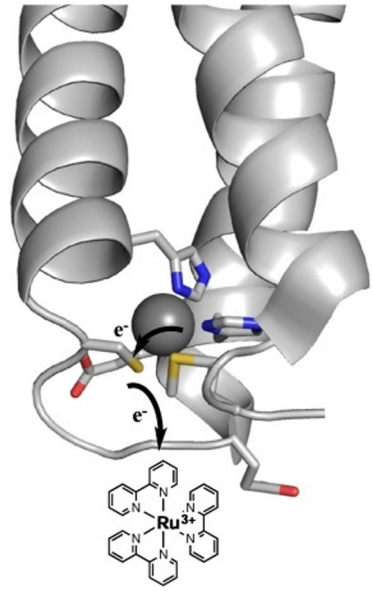

Figure 15. Proposed electron-transfer pathway. For Cuα3DCH3, the Cys residue can provide a super-exchange pathway for electron transfer between the copper center and the photooxidant. Reproduced from Ref. [88b] with permission. Copyright 2018 Elsevier B.V.

Table 9: Intermolecular electron-transfer properties of α_3DCH3.

Sample	$k_{1app}\times10^5$ s^{-1}	$k_{2app}\times10^8$ M^{-1} s^{-1}	Driving force [eV]
Apo α_3DCH3 + Ru(bipy)$_3$	0.39	3.9	
Cuα_3DCH3 + Ru(bipy)$_3$	1.15	6.3	1.18
Cuα_3DCH3 + Ru(phen)$_3$	1.07	10.7	0.88
Cuα_3DCH3 + (COOEt)$_4$Ru(bipy)$_3$	1.08	10.8	1.51
Cuα_3DCH3 + (COOEt)$_2$Ru(bipy)$_3$	1.05	10.5	1.24
Cuα_3DCH3 + ZnTMPyP	0.79	7.9	0.84

between apo-α_3DCH and $[Ru^{III}(bipy)_3]^{3+}$ was due to the presence of redox active residues Cys21, His18/28, and Met72 near the C-terminus of the peptide and, due to its relatively low potential, Cys21 was the most likely candidate. This is consistent with native cupredoxins, in which the Cu–Cys bond acts as an electron conduit.

Bimolecular rate constants for the electron transfer from $Cu^I\alpha_3$DCH to various photooxidants was 8 to $11\times10^8\,M^{-1}s^{-1}$, which indicates diffusion-controlled kinetics and is comparable with native cupredoxins under similar conditions, thus exemplifying the success of this de novo cupredoxin model. Finally, a comparison of rate constant with the driving force of five different photooxidants enabled us to calculate the reorganization energy of Cuα_3DCH3 as 1.1 eV. This is on the higher end of the range seen for native cupredoxins (0.7–1.2 eV).[89]

By comparing with small-molecule complexes such as $[Cu(phen)_2]^{2+}$, whose geometry changes from tetrahedral to pure tetragonal with a reorganization energy of 2.4 eV, we hypothesized that Cuα_3DCH was likely distorting from a pseudo-tetrahedral to pseudo-tetragonal geometry. These results further emphasize that future designs should focus on forcing the Cu^{II} geometry of the construct into an entatic state such as in native blue copper proteins, as previous studies indicate that our constructs already possess the desired Cu^I geometry.

A self-contained de novo CuNiR model with type 1 and type 2 Cu centers for electron transfer and enzymatic activity, respectively, would require an understanding of how electrons would travel through our constructs from one metal center to another. Electron transfer over long distances (ca. 30 Å) is a requirement in various biological systems, such as photosynthesis and respiration.[90] Such long-distance transfers occur through a series of hops, which reduce the distance required for any single-electron transfer and increases the rate of the overall process.[91] Proteins can facilitate such hops through redox-active amino acids such as Tyr and Trp.[92] The formation of tyrosine radicals, in particular, is a vital part of photosystem II, ribonucleotide reductase, and cytochrome *c* oxidase.[90] Electron transfer through the formation of tyrosine radicals occurs in a proton-coupled fashion because of the large differences in the pK_a values between Tyr (10) and it's radical (−2).[93] The study of natural systems which utilize Tyr radicals is hindered by the complexity of those systems. Previous studies on the formation of Tyr radicals within a designed protein found that a single Tyr radical within an alpha-helical bundle can be stabilized through burial in the hydrophobic interior of the peptide.[94] We covalently attached a $Ru^{II}(bipy)_3$ photooxidant on the C-terminal end of our α_3DH_3 carbonic anhydrase construct to create α_3DH_3-Rubpymal and investigate how Tyr hopping could be utilized within our systems to facilitate long-distance electron transfer (Figure 16).[88b] Based on the solution structure of α_3D, we estimated that the bound Ru and Tyr70 (the closest Tyr) were about 16 Å apart.

Laser flash photolysis was used to investigate the nanosecond timescale electron-transfer reaction and kinetics between the bound Ru and Ty70. The intermolecular electron transfer between the radical $Ru^{II}(bipy)_3$ and the electron acceptor $Ru^{III}(NH_3)_6$ produced the oxidized $Ru^{II}(bipy)_3$ with a second order rate constant of $1.1\times10^9\,M^{-1}s^{-1}$ (half-life 40 ns). A second phase with a rate of $3.3\times10^5\,s^{-1}$ was determined on the basis of the observed absorption maxima at 390 and 410 nm to be the formation of Tyr radicals.[94a,95] The observed rate is consistent with that expected for an electron transfer of 16 Å based on a simplified model of electron tunneling in peptides.[96] Finally, a third phase occurs with a half-life of 210 µs, in which the Tyr radical combined with the electron acceptor $Ru^{III}(NH_3)_6$. The pH-dependence of the second phase determined it to be a proton-coupled electron transfer (PCET), as it was four times faster at pH 9.5 than at 5.0 and the presence of a Tyr radical was confirmed through X-band EPR spectroscopy of a reaction in the presence of the nonreversible electron acceptor $[Co^{III}(NH_3)_5Cl]^{2+}$. Future directions of this model will be to design hydrogen-bonding amino acids around Tyr70 to investigate their effect on the observed PCET rate and the distance-dependence of designed electron-transfer relays. Refining the design of electron-transfer relays within alpha-helical bundle scaffolds will bring us that much closer to our overall goal of a self-contained de novo NiR model.

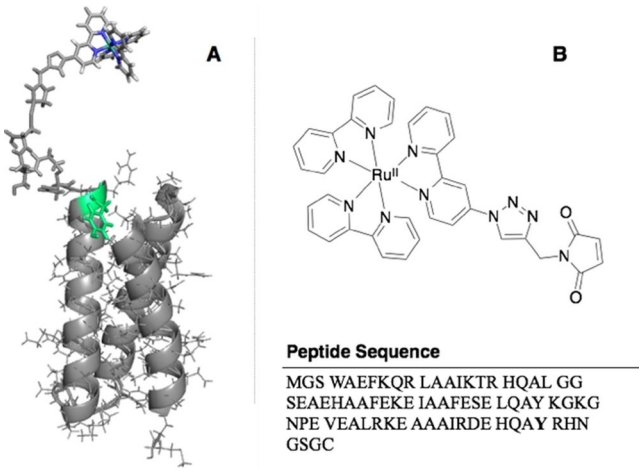

Figure 16. A) Schematic representation of the structure of α_3DH_3-Rubpymal based on the solution NMR structure of a closely related scaffold (PDB: 2MTQ). The key tyrosine residue is marked in green. B) Chemical structure of Rubpymal (top) and sequence of α_3DH_3 (bottom). Reproduced from Ref. [88b] with permission. Copyright 2017 Wiley VCH.

5. Summary and Outlook

This Review summarizes our recent efforts to generate metalloprotein active sites in de novo peptides and proteins composed of three α helices. We have developed several models of metal binding sites with modest to excellent activity compared to the native systems. Specifically, we have, thus far, targeted the hydrolytic activity of zinc bound to symmetric $(His)_3$ environments, copper nitrite reductase activity, and electron-transfer sites within our α-helical scaffolds.

Our approach to generate hydrolytic activity in de novo scaffolds that model the activity of CA, by inserting a tris(his-

tidine) metal binding environment within our well-defined scaffolds, has revealed interesting features of this enzyme. First, much of the activity arises from the symmetric primary coordination sphere being within a peptidic environment. We were able to exceed small-molecule models of CA activity by using native coordinating ligands, in a more native-like system, while still exploring the dependence of activity on the overall protein fold. Although native CA is composed primarily of beta-sheet and loop structures, our completely alien alpha-helical scaffolds described here show modest to excellent CO_2 hydration and pNPA hydrolysis rates. Our next generation hydrolytic active sites will introduce asymmetry in the second coordination sphere, by formation of heterotrimers in our 3SCC system[63] or rational positioning of hydrogen-bonding residues in our α_3DH_3 system. Additionally, we can control the orientation of the amino acid residues in proximity to the metal binding site through the inclusion of non-natural amino acids or noncanonical repeats, such as stutter and stammer inserts, in the heptads.

As with the $Zn(His)_3$ hydrolytic activities, the successful recapitulation of CuNiR activity has, thus far, only included explicit modeling of the primary coordinating ligands, namely the (His_3) environment. As with CA, CuNiRs possess a critical acid-base hydrogen-bonding residue, Asp98, which is required for efficient proton transfer. We had attempted to include Asp in the 3SCC core near the copper site, through L19D or L26D modifications, although evidence suggested that the carboxylates interacted with each other rather than with the copper site. A consequence of working in our self-associating 3SCC is that our modifications are symmetric. It may be possible to generate better CuNiR activities by positioning only a single Asp above or below the copper site. We have recently described a system where we should be able to make these asymmetric modifications in our 3SCC system, by forming heterotrimeric 3SCCs.[63] Inclusion of non-natural amino acids beyond simple methylated histidine should allow us to tune the reduction potentials and Lewis acidity of our metal binding sites.

Finally, we find it interesting to note that rubredoxin and cupredoxin both have binding sites that are comprised of loops. This allows the binding geometry to be largely dictated by the metal rather than the protein matrix. Creating the same metal coordination within the more rigid scaffold of a helical bundle likely requires exact design, which is a limiting factor in our strategy, whereby we replace leucine residues in the layers of the hydrophobic interior, severely limiting the number of geometric arrangements of ligating residues. Thus, further enhancement to the activities of our electron-transfer sites will require specific design of the loop regions that connect the helices in α_3D or $GR\alpha_3D$, or a new scaffold that possesses additional inherent flexibility or secondary structure elements amenable to modification.

Protein design is a powerful tool to both challenge our understanding of metalloprotein systems and expand our knowledge of metalloenzymatic activity. The ability to recapitulate native metalloprotein function in a vastly different protein architecture, both for catalytic and electron-transfer metal sites, highlights a possible pathway for the evolutionary development of the various metalloproteins that are essential for so many cellular functions.

Acknowledgements

T.B.J.P thanks the National Science Research Council of Canada for support in the form of a Postdoctoral Fellowship. V.L.P. thanks the National Institutes of Health for financial support of this research (ES012236). Use of the Stanford Synchrotron Radiation Lightsource, SLAC National Accelerator Laboratory, is supported by the U.S. Department of Energy, Office of Science, Office of Basic Energy Sciences under Contract No. DE-AC02-76SF00515. The SSRL Structural Molecular Biology Program is supported by the DOE Office of Biological and Environmental Research, and by the National Institutes of Health, National Institute of General Medical Sciences (including P41GM103393). The contents of this publication are solely the responsibility of the authors and do not necessarily represent the official views of NIGMS or NIH.

Conflict of interest

The authors declare no conflict of interest.

How to cite: *Angew. Chem. Int. Ed.* **2020**, *59*, 7678–7699
Angew. Chem. **2020**, *132*, 7750–7773

[1] a) K. J. Waldron, J. C. Rutherford, D. Ford, N. J. Robinson, *Nature* **2009**, *460*, 823; b) I. Bertini, A. Sigel, *Handbook on Metalloproteins*, CRC Press, Boca Raton, FL, **2001**; c) C. Andreini, I. Bertini, G. Cavallaro, G. L. Holliday, J. M. Thornton, *J. Biol. Inorg. Chem.* **2008**, *13*, 1205–1218.
[2] C. Andreini, I. Bertini, A. Rosato, *Acc. Chem. Res.* **2009**, *42*, 1471–1479.
[3] a) P.-S. Huang, S. E. Boyken, D. Baker, *Nature* **2016**, *537*, 320; b) F. Yu, V. M. Cangelosi, M. L. Zastrow, M. Tegoni, J. S. Plegaria, A. G. Tebo, C. S. Mocny, L. Ruckthong, H. Qayyum, V. L. Pecoraro, *Chem. Rev.* **2014**, *114*, 3495–3578; c) Y. Lu, S. M. Berry, T. D. Pfister, *Chem. Rev.* **2001**, *101*, 3047–3080; d) Y. Lu, N. Yeung, N. Sieracki, N. M. Marshall, *Nature* **2009**, *460*, 855; e) F. Nastri, D. D′Alonzo, L. Leone, G. Zambrano, V. Pavone, A. Lombardi, *Trends Biochem. Sci* **2019**, *44*, 1022–1040.
[4] B. A. Smith, M. H. Hecht, *Curr. Opin. Chem. Biol.* **2011**, *15*, 421–426.
[5] J. Kaplan, W. F. DeGrado, *Proc. Natl. Acad. Sci. USA* **2004**, *101*, 11566–11570.
[6] D. N. Woolfson, G. J. Bartlett, A. J. Burton, J. W. Heal, A. Niitsu, A. R. Thomson, C. W. Wood, *Curr. Opin. Struct. Biol.* **2015**, *33*, 16–26.
[7] a) J. P. Schneider, A. Lombardi, W. F. DeGrado, *Fold. Des.* **1998**, *3*, R29–R40; b) E. Moutevelis, D. N. Woolfson, *J. Mol. Biol.* **2009**, *385*, 726–732.
[8] B. Lovejoy, S. Choe, D. Cascio, D. McRorie, W. F. DeGrado, D. Eisenberg, *Science* **1993**, *259*, 1288–1293.
[9] R. S. Hodges, A. K. Saund, P. C. Chong, S. A. St-Pierre, R. E. Reid, *J. Biol. Chem.* **1981**, *256*, 1214–1224.
[10] G. R. Dieckmann, D. K. McRorie, D. L. Tierney, L. M. Utschig, C. P. Singer, T. V. O'Halloran, J. E. Penner-Hahn, W. F. DeGrado, V. L. Pecoraro, *J. Am. Chem. Soc.* **1997**, *119*, 6195–6196.

[11] K. J. Koebke, L. Ruckthong, J. L. Meagher, E. Mathieu, J. Harland, A. Deb, N. Lehnert, C. Policar, C. Tard, J. E. Penner-Hahn, *Inorg. Chem.* **2018**, *57*, 12291 – 12302.

[12] M. L. Zastrow, A. F. Peacock, J. A. Stuckey, V. L. Pecoraro, *Nat. Chem.* **2012**, *4*, 118.

[13] J. S. Plegaria, S. P. Dzul, E. R. Zuiderweg, T. L. Stemmler, V. L. Pecoraro, *Biochemistry* **2015**, *54*, 2858 – 2873.

[14] R. H. Holm, P. Kennepohl, E. I. Solomon, *Chem. Rev.* **1996**, *96*, 2239 – 2314.

[15] a) J. Liu, S. Chakraborty, P. Hosseinzadeh, Y. Yu, S. Tian, I. Petrik, A. Bhagi, Y. Lu, *Chem. Rev.* **2014**, *114*, 4366 – 4469; b) S. Shaik, A. W. Munro, S. Sen, C. Mowat, W. Nam, E. Derat, T. Bugg, D. A. Proshlyakov, R. P. Hausinger, G. D. Straganz, *Iron-containing enzymes: Versatile catalysts of hydroxylation reactions in nature*, Royal Society of Chemistry, London, **2011**; c) R. Lill, *Nature* **2009**, *460*, 831; d) C. Andreini, V. Putignano, A. Rosato, L. Banci, *Metallomics* **2018**, *10*, 1223 – 1231.

[16] a) K.-H. Lee, M. Matzapetakis, S. Mitra, E. N. G. Marsh, V. L. Pecoraro, *J. Am. Chem. Soc.* **2004**, *126*, 9178 – 9179; b) L. Ruckthong, A. Deb, L. Hemmingsen, J. E. Penner-Hahn, V. L. Pecoraro, *J. Biol. Inorg. Chem.* **2018**, *23*, 123 – 135; c) A. F. Peacock, L. Hemmingsen, V. L. Pecoraro, *Proc. Natl. Acad. Sci. USA* **2008**, *105*, 16566 – 16571; d) A. F. Peacock, J. A. Stuckey, V. L. Pecoraro, *Angew. Chem. Int. Ed.* **2009**, *48*, 7371 – 7374; *Angew. Chem.* **2009**, *121*, 7507 – 7510.

[17] K. Håkansson, M. Carlsson, L. A. Svensson, A. Liljas, *J. Mol. Biol.* **1992**, *227*, 1192 – 1204.

[18] a) E. Kimura, T. Shiota, T. Koike, M. Shiro, M. Kodama, *J. Am. Chem. Soc.* **1990**, *112*, 5805 – 5811; b) C. P. Olmo, K. Böhmerle, H. Vahrenkamp, *Inorg. Chim. Acta* **2007**, *360*, 1510 – 1516; c) T. B. Koerner, R. Brown, *Can. J. Chem.* **2002**, *80*, 183 – 191.

[19] a) L. L. Kiefer, S. A. Paterno, C. A. Fierke, *J. Am. Chem. Soc.* **1995**, *117*, 6831 – 6837; b) J. F. Krebs, J. Ippolito, D. Christianson, C. Fierke, *J. Biol. Chem.* **1993**, *268*, 27458 – 27466; c) Z. Liang, Y. Xue, G. Behravan, B. H. Jonsson, S. Lindskog, *Eur. J. Biochem.* **1993**, *211*, 821 – 827.

[20] B. S. Der, D. R. Edwards, B. Kuhlman, *Biochemistry* **2012**, *51*, 3933 – 3940.

[21] M. L. Zastrow, V. L. Pecoraro, *J. Am. Chem. Soc.* **2013**, *135*, 5895 – 5903.

[22] A. E. Eriksson, T. A. Jones, A. Liljas, *Proteins Struct. Funct. Bioinf.* **1988**, *4*, 274 – 282.

[23] M. Matzapetakis, B. T. Farrer, T.-C. Weng, L. Hemmingsen, J. E. Penner-Hahn, V. L. Pecoraro, *J. Am. Chem. Soc.* **2002**, *124*, 8042 – 8054.

[24] V. M. Cangelosi, A. Deb, J. E. Penner-Hahn, V. L. Pecoraro, *Angew. Chem. Int. Ed.* **2014**, *53*, 7900 – 7903; *Angew. Chem.* **2014**, *126*, 8034 – 8037.

[25] J. E. Jackman, K. M. Merz, C. A. Fierke, *Biochemistry* **1996**, *35*, 16421 – 16428.

[26] D. A. Jewell, C. Tu, S. R. Paranawithana, S. M. Tanhauser, P. V. LoGrasso, P. J. Laipis, D. N. Silverman, *Biochemistry* **1991**, *30*, 1484 – 1490.

[27] L. Koziol, C. A. Valdez, S. E. Baker, E. Y. Lau, W. C. Floyd III, S. E. Wong, J. H. Satcher, Jr, F. C. Lightstone, R. D. Aines, *Inorg. Chem.* **2012**, *51*, 6803 – 6812.

[28] K. Nakata, N. Shimomura, N. Shiina, M. Izumi, K. Ichikawa, M. Shiro, *J. Inorg. Biochem.* **2002**, *89*, 255 – 266.

[29] H. Slebocka-Tilk, J. Cocho, Z. Frackman, R. Brown, *J. Am. Chem. Soc.* **1984**, *106*, 2421 – 2431.

[30] C. A. Fierke, T. L. Calderone, J. F. Krebs, *Biochemistry* **1991**, *30*, 11054 – 11063.

[31] S. Studer, D. A. Hansen, Z. L. Pianowski, P. R. Mittl, A. Debon, S. L. Guffy, B. S. Der, B. Kuhlman, D. Hilvert, *Science* **2018**, *362*, 1285 – 1288.

[32] a) W. J. Song, F. A. Tezcan, *Science* **2014**, *346*, 1525 – 1528; b) J. D. Brodin, A. Medina-Morales, T. Ni, E. N. Salgado, X. I. Ambroggio, F. A. Tezcan, *J. Am. Chem. Soc.* **2010**, *132*, 8610 – 8617.

[33] C. M. Rufo, Y. S. Moroz, O. V. Moroz, J. Stöhr, T. A. Smith, X. Hu, W. F. DeGrado, I. V. Korendovych, *Nat. Chem.* **2014**, *6*, 303.

[34] L. Ruckthong, M. L. Zastrow, J. A. Stuckey, V. L. Pecoraro, *J. Am. Chem. Soc.* **2016**, *138*, 11979 – 11988.

[35] a) H. Iwasaki, S. Noji, S. Shidara, *J. Biochem.* **1975**, *78*, 355 – 361; b) E. Libby, B. A. Averill, *Biochem. Biophys. Res. Commun.* **1992**, *187*, 1529 – 1535; c) M. Kukimoto, M. Nishiyama, M. E. Murphy, S. Turley, E. T. Adman, S. Horinouchi, T. Beppu, *Biochemistry* **1994**, *33*, 5246 – 5252; d) M. E. Murphy, S. Turley, E. T. Adman, *J. Biol. Chem.* **1997**, *272*, 28455 – 28460.

[36] a) S. V. Antonyuk, R. W. Strange, G. Sawers, R. R. Eady, S. S. Hasnain, *Proc. Natl. Acad. Sci. USA* **2005**, *102*, 12041 – 12046; b) K. Kataoka, H. Furusawa, K. Takagi, K. Yamaguchi, S. Suzuki, *J. Biochem.* **2000**, *127*, 345 – 350; c) M. J. Boulanger, M. Kukimoto, M. Nishiyama, S. Horinouchi, M. E. Murphy, *J. Biol. Chem.* **2000**, *275*, 23957 – 23964.

[37] M. Tegoni, F. Yu, M. Bersellini, J. E. Penner-Hahn, V. L. Pecoraro, *Proc. Natl. Acad. Sci. USA* **2012**, *109*, 21234 – 21239.

[38] L. S. Kau, D. J. Spira-Solomon, J. E. Penner-Hahn, K. O. Hodgson, E. I. Solomon, *J. Am. Chem. Soc.* **1987**, *109*, 6433 – 6442.

[39] E. Prenesti, P. G. Daniele, M. Prencipe, G. Ostacoli, *Polyhedron* **1999**, *18*, 3233 – 3241.

[40] K. Olesen, A. Veselov, Y. Zhao, Y. Wang, B. Danner, C. P. Scholes, J. P. Shapleigh, *Biochemistry* **1998**, *37*, 6086 – 6094.

[41] a) F. Jacobson, A. Pistorius, D. Farkas, W. De Grip, Ö. Hansson, L. Sjölin, R. Neutze, *J. Biol. Chem.* **2007**, *282*, 6347 – 6355; b) S. Suzuki, K. Yamaguchi, K. Kataoka, K. Kobayashi, S. Tagawa, T. Kohzuma, S. Shidara, H. Iwasaki, *J. Biol. Inorg. Chem.* **1997**, *2*, 265 – 274.

[42] E. Monzani, G. A. A. Koolhaas, A. Spandre, E. Leggieri, L. Casella, M. Gullotti, G. Nardin, L. Randaccio, M. Fontani, P. Zanello, *J. Biol. Inorg. Chem.* **2000**, *5*, 251 – 261.

[43] A. Warshel, P. K. Sharma, M. Kato, Y. Xiang, H. Liu, M. H. Olsson, *Chem. Rev.* **2006**, *106*, 3210 – 3235.

[44] S. D. Fried, S. Bagchi, S. G. Boxer, *Science* **2014**, *346*, 1510 – 1514.

[45] a) R. Zwanzig, *J. Chem. Phys.* **1992**, *97*, 3587 – 3589; b) W. Min, B. P. English, G. Luo, B. J. Cherayil, S. Kou, X. S. Xie, *Acc. Chem. Res.* **2005**, *38*, 923 – 931.

[46] M. R. Ross, A. M. White, F. Yu, J. T. King, V. L. Pecoraro, K. J. Kubarych, *J. Am. Chem. Soc.* **2015**, *137*, 10164 – 10176.

[47] M. Lim, P. Hamm, R. M. Hochstrasser, *Proc. Natl. Acad. Sci. USA* **1998**, *95*, 15315 – 15320.

[48] a) A. Churg, A. Warshel, *Biochemistry* **1986**, *25*, 1675 – 1681; b) D. Kuila, J. A. Fee, *J. Biol. Chem.* **1986**, *261*, 2768 – 2771; c) R. Varadarajan, T. E. Zewert, H. B. Gray, S. G. Boxer, *Science* **1989**, *243*, 69 – 72.

[49] E. E. Chufán, S. T. Prigge, X. Siebert, B. A. Eipper, R. E. Mains, L. M. Amzel, *J. Am. Chem. Soc.* **2010**, *132*, 15565 – 15572.

[50] F. Yu, J. E. Penner-Hahn, V. L. Pecoraro, *J. Am. Chem. Soc.* **2013**, *135*, 18096 – 18107.

[51] H. B. Gray, B. G. Malmström, *Comments Inorg. Chem.* **1983**, *2*, 203 – 209.

[52] a) O. Iranzo, C. Cabello, V. L. Pecoraro, *Angew. Chem. Int. Ed.* **2007**, *46*, 6688 – 6691; *Angew. Chem.* **2007**, *119*, 6808 – 6811; b) K. H. Lee, C. Cabello, L. Hemmingsen, E. N. G. Marsh, V. L. Pecoraro, *Angew. Chem. Int. Ed.* **2006**, *45*, 2864 – 2868; *Angew. Chem.* **2006**, *118*, 2930 – 2934.

[53] K. J. Koebke, F. Yu, E. Salerno, C. Van Stappen, A. G. Tebo, J. E. Penner-Hahn, V. L. Pecoraro, *Angew. Chem. Int. Ed.* **2018**, *57*, 3954 – 3957; *Angew. Chem.* **2018**, *130*, 4018 – 4021.

[54] Y. Fukuda, K. M. Tse, T. Nakane, T. Nakatsu, M. Suzuki, M. Sugahara, S. Inoue, T. Masuda, F. Yumoto, N. Matsugaki, *Proc. Natl. Acad. Sci. USA* **2016**, *113*, 2928 – 2933.

[55] S. T. Prigge, A. S. Kolhekar, B. A. Eipper, R. E. Mains, L. M. Amzel, *Science* **1997**, *278*, 1300 – 1305.

[56] K. J. Koebke, F. Yu, C. Van Stappen, T. B. Pinter, A. Deb, J. E. Penner-Hahn, V. L. Pecoraro, *J. Am. Chem. Soc.* **2019**, *141*, 7765 – 7775.

[57] M. Tanokura, *Biochim. Biophys. Acta Protein Struct. Mol. Enzymol.* **1983**, *742*, 576 – 585.

[58] M. Tegoni, F. Yu, M. Bersellini, J. E. Penner-Hahn, V. L. Pecoraro, *Proc. Natl. Acad. Sci. USA* **2012**, *109*, 21234 – 21239.

[59] K. J. Koebke, F. Yu, E. Salerno, C. V. Stappen, A. G. Tebo, J. E. Penner-Hahn, V. L. Pecoraro, *Angew. Chem. Int. Ed.* **2018**, *57*, 3954 – 3957; *Angew. Chem.* **2018**, *130*, 4018 – 4021.

[60] N. Isoda, H. Yokoyama, M. Nojiri, S. Suzuki, K. Yamaguchi, *Bioelectrochemistry* **2010**, *77*, 82 – 88.

[61] E. I. Tocheva, L. D. Eltis, M. E. P. Murphy, *Biochemistry* **2008**, *47*, 4452 – 4460.

[62] N. G. H. Leferink, C. Han, S. V. Antonyuk, D. J. Heyes, S. E. J. Rigby, M. A. Hough, R. R. Eady, N. S. Scrutton, S. S. Hasnain, *Biochemistry* **2011**, *50*, 4121 – 4131.

[63] A. E. Tolbert, C. S. Ervin, L. Ruckthong, T. J. Paul, V. M. Jayasinghe-Arachchige, K. P. Neupane, J. A. Stuckey, R. Prabhakar, V. L. Pecoraro, *Nat. Chem.* **2019**, in press.

[64] a) W. Lovenberg, B. E. Sobel, *Proc. Natl. Acad. Sci. USA* **1965**, *54*, 193 – 199; b) P. Bertrand, J.-P. Gayda, *Biochim. Biophys. Acta Protein Struct. Mol. Enzymol.* **1988**, *954*, 347 – 350; c) R. G. Shulman, P. Eisenberger, W. E. Blumberg, N. A. Stombaugh, *Proc. Natl. Acad. Sci. USA* **1975**, *72*, 4003 – 4007; d) B. Bunker, E. A. Stern, *Biophys. J.* **1977**, *19*, 253 – 264; e) N. M. Atherton, K. Garbett, R. D. Gillard, R. Mason, S. J. Mayhew, J. L. Peel, J. E. Stangroom, *Nature* **1966**, *212*, 590 – 593; f) H. Bönisch, C. L. Schmidt, P. Bianco, R. Ladenstein, *J. Biol. Inorg. Chem.* **2007**, *12*, 1163 – 1171.

[65] a) S. C. Lee, W. Lo, R. H. Holm, *Chem. Rev.* **2014**, *114*, 3579 – 3600; b) D. L. Gerlach, D. Coucouvanis, J. Kampf, N. Lehnert, *Eur. J. Inorg. Chem.* **2013**, 5253 – 5264.

[66] a) A. Jacques, M. Clémancey, G. Blondin, V. Fourmond, J.-M. Latour, O. Sénèque, *Chem. Commun.* **2013**, *49*, 2915 – 2917; b) V. Nanda, M. M. Rosenblatt, A. Osyczka, H. Kono, Z. Getahun, P. L. Dutton, J. G. Saven, W. F. DeGrado, *J. Am. Chem. Soc.* **2005**, *127*, 5804 – 5805; c) A. Jacques, J.-M. Latour, O. Sénèque, *Dalton Trans.* **2014**, *43*, 3922 – 3930; d) E. Farinas, L. Regan, *Protein Sci.* **1998**, *7*, 1939 – 1946; e) D. E. Benson, M. S. Wisz, W. Liu, H. W. Hellinga, *Biochemistry* **1998**, *37*, 7070 – 7076.

[67] A. G. Tebo, T. B. J. Pinter, R. García-Serres, A. L. Speelman, C. Tard, O. Sénéque, G. Blondin, J.-M. Latour, J. Penner-Hahn, N. Lehnert, V. L. Pecoraro, *Biochemistry* **2018**, *57*, 2308 – 2316.

[68] A. G. Tebo, L. Hemmingsen, V. L. Pecoraro, *Metallomics* **2015**, *7*, 1555 – 1561.

[69] Z. Xiao, M. J. Lavery, M. Ayhan, S. D. B. Scrofani, M. C. J. Wilce, J. M. Guss, P. A. Tregloan, G. N. George, A. G. Wedd, *J. Am. Chem. Soc.* **1998**, *120*, 4135 – 4150.

[70] a) P. Wegner, M. Bever, V. Schünemann, A. X. Trautwein, C. Schmidt, H. Bönisch, M. Gnida, W. Meyer-Klaucke, *Hyperfine Interact.* **2004**, *156*, 293 – 298; b) J. M. Meyer, in *Handbook of Metalloproteins* (Ed.: A. H. Messerschmidt, R. Poulat, T. Wieghardt), Wiley, Hoboken, **2006**.

[71] a) I. Moura, A. V. Xavier, R. Cammack, M. Bruschi, J. Le Gall, *Biochim. Biophys. Acta Protein Struct.* **1978**, *533*, 156 – 162; b) F. E. Jenney, M. W. W. Adams, in *Methods Enzymol.*, *Vol. 334*, Academic Press, San Diego, **2001**, pp. 45 – 55.

[72] a) V. S. Oganesyan, S. J. George, M. R. Cheesman, A. J. Thomson, *J. Chem. Phys.* **1999**, *110*, 762 – 777; b) S. J. Yoo, J. Meyer, C. Achim, J. Peterson, M. P. Hendrich, E. Münck, *J. Biol. Inorg. Chem.* **2000**, *5*, 475 – 487; c) B. Börger, D. Suter, *J. Chem. Phys.* **2001**, *115*, 9821 – 9826; d) J. Peisach, W. E. Blumberg, E. T. Lode, M. J. Coon, *J. Biol. Chem.* **1971**, *246*, 5877 – 5881.

[73] E. I. Solomon, *Inorg. Chem.* **2006**, *45*, 8012 – 8025.

[74] A. A. Gewirth, E. I. Solomon, *J. Am. Chem. Soc.* **1988**, *110*, 3811 – 3819.

[75] L. B. LaCroix, S. E. Shadle, Y. Wang, B. A. Averill, B. Hedman, K. O. Hodgson, E. I. Solomon, *J. Am. Chem. Soc.* **1996**, *118*, 7755 – 7768.

[76] L. Basumallick, R. Sarangi, S. DeBeer George, B. Elmore, A. B. Hooper, B. Hedman, K. O. Hodgson, E. I. Solomon, *J. Am. Chem. Soc.* **2005**, *127*, 3531 – 3544.

[77] a) H. W. Hellinga, *J. Am. Chem. Soc.* **1998**, *120*, 10055 – 10066; b) Y. Lu, L. B. LaCroix, M. D. Lowery, E. I. Solomon, C. J. Bender, J. Peisach, J. A. Roe, E. B. Gralla, J. S. Valentine, *J. Am. Chem. Soc.* **1993**, *115*, 5907 – 5918; c) R. Schnepf, W. Haehnel, K. Wieghardt, P. Hildebrandt, *J. Am. Chem. Soc.* **2004**, *126*, 14389 – 14399; d) D. Shiga, D. Nakane, T. Inomata, Y. Funahashi, H. Masuda, A. Kikuchi, M. Oda, M. Noda, S. Uchiyama, K. Fukui, K. Kanaori, K. Tajima, Y. Takano, H. Nakamura, T. Tanaka, *J. Am. Chem. Soc.* **2010**, *132*, 18191 – 18198.

[78] D. Shiga, Y. Hamano, M. Kamei, Y. Funahashi, H. Masuda, M. Sakaguchi, T. Ogura, T. Tanaka, *J. Biol. Inorg. Chem.* **2012**, *17*, 1025 – 1031.

[79] J. S. Plegaria, M. Duca, C. Tard, T. J. Friedlander, A. Deb, J. E. Penner-Hahn, V. L. Pecoraro, *Inorg. Chem.* **2015**, *54*, 9470 – 9482.

[80] S. Chakraborty, J. Y. Kravitz, P. W. Thulstrup, L. Hemmingsen, W. F. DeGrado, V. L. Pecoraro, *Angew. Chem. Int. Ed.* **2011**, *50*, 2049 – 2053; *Angew. Chem.* **2011**, *123*, 2097 – 2101.

[81] a) K. W. Penfield, R. R. Gay, R. S. Himmelwright, N. C. Eickman, V. A. Norris, H. C. Freeman, E. I. Solomon, *J. Am. Chem. Soc.* **1981**, *103*, 4382 – 4388; b) G. P. Anderson, D. G. Sanderson, C. H. Lee, S. Durell, L. B. Anderson, E. L. Gross, *Biochim. Biophys. Acta* **1987**, *894*, 386 – 398.

[82] D. M. Arciero, B. S. Pierce, M. P. Hendrich, A. B. Hooper, *Biochemistry* **2002**, *41*, 1703 – 1709.

[83] a) B. G. Karlsson, L.-C. Tsai, H. Nar, J. Sanders-Loehr, N. Bonander, V. Langer, L. Sjölin, *Biochemistry* **1997**, *36*, 4089 – 4095; b) J. F. Hall, L. D. Kanbi, R. W. Strange, S. S. Hasnain, *Biochemistry* **1999**, *38*, 12675 – 12680.

[84] a) T. Pascher, B. G. Karlsson, M. Nordling, B. G. Malmstom, T. Vanngard, *Eur. J. Biochem.* **1993**, *212*, 289 – 296; b) A. G. Lappin, C. A. Lewis, W. J. Ingledew, *Inorg. Chem.* **1985**, *24*, 1446 – 1450; c) F. Xu, R. M. Berka, J. A. Wahleithner, B. A. Nelson, J. R. Shuster, S. H. Brown, A. E. Palmer, E. I. Solomon, *Biochem. J.* **1998**, *334*, 63 – 70.

[85] a) B. T. Farrer, N. P. Harris, K. E. Balchus, V. L. Pecoraro, *Biochemistry* **2001**, *40*, 14696 – 14705; b) J. Y. Su, R. S. Hodges, C. M. Kay, *Biochemistry* **1994**, *33*, 15501 – 15510.

[86] S. Tian, J. Liu, R. E. Cowley, P. Hosseinzadeh, N. M. Marshall, Y. Yu, H. Robinson, M. J. Nilges, N. J. Blackburn, E. I. Solomon, Y. Lu, *Nat. Chem.* **2016**, *8*, 670 – 677.

[87] K. J. Koebke, T. B. J. Pinter, A. Deb, C. Tard, J. Penner-Hahn, V. L. Pecoraro, unpublished results.

[88] a) J. S. Plegaria, C. Herrero, A. Quaranta, V. L. Pecoraro, *Biochim. Biophys. Acta Bioenerg.* **2016**, *1857*, 522 – 530; b) A. G. Tebo, A. Quaranta, C. Herrero, V. L. Pecoraro, A. Aukauloo, *ChemPhotoChem* **2017**, *1*, 89 – 92.

[89] a) J. R. Winkler, P. Wittung-Stafshede, J. Leckner, B. G. Malmström, H. B. Gray, *Proc. Natl. Acad. Sci. USA* **1997**, *94*, 4246 – 4249; b) A. J. Di Bilio, M. G. Hill, N. Bonander, B. G. Karlsson, R. M. Villahermosa, B. G. Malmström, J. R. Winkler, H. B. Gray, *J. Am. Chem. Soc.* **1997**, *119*, 9921 – 9922; c) L. K. Skov, T. Pascher, J. R. Winkler, H. B. Gray, *J. Am. Chem. Soc.* **1998**, *120*, 1102 – 1103; d) K. Sigfridsson, M. Ejdebäck, M. Sundahl, Ö. Hansson, *Arch. Biochem. Biophys.* **1998**, *351*, 197 – 206; e) T. M. McCleskey, J. R. Winkler, H. B. Gray, *J. Am. Chem. Soc.* **1992**, *114*, 6935 – 6937.

[90] J. L. Dempsey, J. R. Winkler, H. B. Gray, *Chem. Rev.* **2010**, *110*, 7024 – 7039.

[91] a) H. B. Gray, J. R. Winkler, *Chem. Phys. Lett.* **2009**, *483*, 1 – 9; b) H. B. Gray, J. R. Winkler, *Q. Rev. Biophys.* **2003**, *36*, 341 – 372;

c) C. C. Moser, J. M. Keske, K. Warncke, R. S. Farid, P. L. Dutton, *Nature* **1992**, *355*, 796 – 802.
[92] B. A. Barry, *J. Photochem. Photobiol. B* **2011**, *104*, 60 – 71.
[93] W. T. Dixon, D. Murphy, *J. Chem. Soc. Faraday Trans. 2* **1976**, *72*, 1221 – 1230.
[94] a) B. W. Berry, M. C. Martínez-Rivera, C. Tommos, *Proc. Natl. Acad. Sci. USA* **2012**, *109*, 9739 – 9743; b) S. D. Glover, C. Jorge, L. Liang, K. G. Valentine, L. Hammarström, C. Tommos, *J. Am. Chem. Soc.* **2014**, *136*, 14039 – 14051.
[95] a) L. P. Candeias, S. Turconi, J. H. A. Nugent, *Biochim. Biophys. Acta Bioenerg.* **1998**, *1363*, 1 – 5; b) A. A. Pizano, D. A. Lutterman, P. G. Holder, T. S. Teets, J. Stubbe, D. G. Nocera, *Proc. Natl. Acad. Sci. USA* **2012**, *109*, 39 – 43.
[96] C. C. Moser, P. L. Dutton, *Biochim. Biophys. Acta Bioenerg.* **1992**, *1101*, 171 – 176.

Manuscript received: June 16, 2019
Accepted manuscript online: August 22, 2019
Version of record online: March 2, 2020

